Spatial and Temporal Distribution of Clouds Observed by MODIS onboard the Terra and Aqua Satellites

Michael D. King, *Senior Member*, *IEEE*, Steven Platnick, W. Paul Menzel,
Steven A. Ackerman, and Paul A. Hubanks

IEEE Transactions on Geoscience and Remote Sensing

Manuscript submitted April 30, 2012.

M. D. King is with the Laboratory for Atmospheric and Space Physics, University of Colorado Boulder, 3665 Discovery Dr., Boulder, CO 80303-7819 USA (e-mail: michael.king@lasp.colorado.edu).

S. Platnick is with the Earth Sciences Division, NASA Goddard Space Flight Center, Greenbelt, MD 20771 USA.

W. P. Menzel and S. A. Ackerman are with the Cooperative Institute for Meteorological Satellite Studies, University of Wisconsin, Madison, WI 53706 USA.

P. A. Hubanks is with Science Systems and Applications, Inc., Seabrook, MD 20706 USA.

Abstract—The Moderate Resolution Imaging Spectroradiometer (MODIS) was developed by NASA and launched aboard the *Terra* spacecraft on December 18, 1999 and *Aqua* spacecraft on May 4, 2002. A comprehensive set of remote sensing algorithms for the retrieval of cloud physical and optical properties have enabled over twelve years of continuous observations of cloud properties from *Terra* and over nine years from *Aqua*. The archived products from these algorithms include 1 km pixel-level (Level-2) and global gridded Level-3 products. In addition to an extensive cloud mask, products include cloud-top properties (temperature, pressure, effective emissivity), cloud thermodynamic phase, cloud optical and microphysical parameters (optical thickness, effective particle radius, water path), as well as derived statistics. Results include the latitudinal distribution of cloud optical and radiative properties for both liquid water and ice clouds, as well as latitudinal distributions of cloud top pressure and cloud top temperature.

MODIS finds the cloud fraction, as derived by the cloud mask, is nearly identical during the day and night, with only modest diurnal variation. Globally, the cloud fraction derived by the MODIS cloud mask is ~67%, with somewhat more clouds over land during the afternoon and less clouds over ocean in the afternoon, with very little difference in global cloud cover between *Terra* and *Aqua*. Overall, cloud fraction over land is ~55%, with a distinctive seasonal cycle, whereas the ocean cloudiness is much higher, around 72%, with much reduced seasonal variation.

Cloud top pressure and temperature have distinct spatial and temporal patterns, and clearly reflect our understanding of the global cloud distribution. High clouds are especially prevalent over the northern hemisphere continents between 30° and 50°. *Aqua* and *Terra* have comparable zonal cloud top pressures, with *Aqua* having somewhat higher clouds (cloud top pressures lower by 100 hPa) over land due to afternoon deep convection. The coldest cloud tops (colder than 230 K) generally occur over Antarctica and the high clouds in the tropics (ITCZ and the deep convective clouds over the western tropical Pacific and Indian sub-continent). The cold clouds over the Sahara, though infrequent,

are generally high, thin cirrus.

The cloud effective particle radius of liquid water clouds is significantly larger over ocean (mode 12-13 μm) than land (mode 10-11 μm), consistent with the variation in hydroscopic aerosol concentrations that provide cloud condensation nuclei necessary for cloud formation. We also find the effective radius to be 2-3 μm larger in the southern hemisphere than the northern hemisphere, likely reflecting differences in sources of cloud condensation nuclei.

Index Terms—Aqua, clouds, cloud remote sensing, satellite applications, *Terra*, terrestrial atmosphere, Moderate Resolution Imaging Spectroradiometer (MODIS).

I. Introduction

The Moderate Resolution Imaging Spectroradiometer (MODIS) is an instrument that is currently flying aboard the *Terra* and *Aqua* spacecraft. In addition to its use in the global monitoring of terrestrial ecosystems, fires, ocean biological properties, and sea surface temperature, it is well-suited to the monitoring of atmospheric properties from space. The wide spectral range (0.41–14.24 μm), frequent global coverage (one to two days revisit), and two high spatial resolution bands (250 m), permit state-of-the-art global monitoring of atmospheric profiles, column water vapor amount, aerosol particles, and the subsequently formed clouds [11], [12]. Barnes *et al.* [3] provide a detailed description of MODIS, including its performance attributes, optical design, spectral band characteristics, primary purpose of each band, pixel size, and signal-to-noise ratios at specified radiance levels, information that is essential for an in-depth understanding of the onboard calibrators and the operation of this highly sophisticated sensor. MODIS is a whiskbroom scanner with 36 spectral bands on four focal plane assemblies that image the earth in a swath 2330 km cross-track and 10 km along-track for each sweep of the scan mirror. Each band's spectral response is determined by an interference filter overlying a detector array and each 10-km swath along-track is imaged on 40, 20, and 10 element arrays for the 250, 500, and 1-km bands, respectively. There are a total of 470 detectors on the four focal planes, and much effort is expended in characterizing and monitoring the calibration and performance of each detector as it sweeps out an image, with extra attention being played to the reflectance and emission characteristics of each side of the scan mirror [50], [51].

The global distribution of clouds and their physical and optical properties have been derived from this sensor since February 24, 2000, when the first analysis of *Terra*/MODIS data became available. Prior to the launch of *Terra*, cloud properties had been derived from a wide variety of sensors from aircraft [28], [5], [36], [14] as well as satellite [19],

[41], [47], [7], [35], [30], [40], [48], [49], but the advent of MODIS, with its wide spectral coverage and high spatial resolution, has enabled additional cloud properties to be derived that were previously unattainable.

Among the most popular 'cloud properties' for the climate modeling community is cloud cover, or cloud fraction, though this is an ill-defined property that depends very heavily on the spatial resolution of the sensor (due to partially-filled fields of view) and radiometric sensitivity (minimum detection limit). The International Satellite Cloud Climatology Project (ISCCP) used only two wavelengths to detect clouds, one visible and one infrared, and used geosynchronous satellites as the preferred satellite source except at high latitudes [40], [41]. Early Advanced Very High Resolution Radiometer (AVHRR) algorithms used, at most, five spectral channels, as that was all that was available on this sensor, but the operational cloud mask algorithm was developed as a unified cloud mask algorithm for ocean, land, and atmosphere applications [42]. Minnis *et al.* [24] developed a cloud mask to identify clouds using primarily 4 wavelengths from the Visible and Infrared Scanner (VIRS) on the Tropical Rainfall Measuring Mission (TRMM) and MODIS on *Terra* and *Aqua*, supplemented by at most 2 additional bands on *Aqua*. With the advent of MODIS, and its extended wavelength range and high radiometric accuracy, Ackerman *et al.* [1] and Frey *et al.* [6] developed a cloud mask algorithm that utilizes up to 22 spectral bands, but uses different bands for daytime and nighttime and for various surface conditions (snow, land, ocean, desert, and coastal). These various choices lead to somewhat different cloud fractions, but the increasing skill over time has allowed a very high confidence in cloud detection for all clouds of optical thickness > 0.4 [2].

In addition to cloud fraction, the MODIS atmosphere team has developed algorithms for cloud top pressure, cloud top temperature, thermodynamic phase, as well as cloud optical thickness, effective radius, and water path of liquid water and ice clouds [37], [20], [16]. There are many similarities as well as substantial differences between

these results and those derived independently by the Clouds and the Earth's Radiant Energy System (CERES) that makes use of the same MODIS instrument but a restricted set of spectral bands [22], [23]. This MODIS-CERES product is used within the CERES processing system to support cloud radiation budget and cloud forcing assessments, but having an independent analysis of cloud properties has value in enhancing and improving our understanding of the cloud radiative properties of the Earth's atmosphere.

MODIS data are processed into various processing levels from Level-1 (radiances and brightness temperatures that have been geolocated), to Level-2 (derived geophysical data products at the same resolution and location as the Level-1 data) to Level-3 (retrievals aggregated onto uniform space-time grid scales). The intent of this paper is to explain how the Level-3 products are produced in Collection 5 processing and discuss results from both *Terra* and *Aqua*. We begin by briefly describing the essential elements of all Level-2 'pixel-based' MODIS cloud products. We then describe the MODIS Level-3 cloud products that are produced at monthly time intervals on a global 1° x 1° latitude-longitude grid. In addition to simple statistics (mean, standard deviation, etc.) computed for each parameter, the Level-3 products also contain marginal probability density functions (histograms) and joint probability density functions (joint histograms) between selected parameters. We will illustrate seasonal, zonal, and spatial characteristics of these cloud properties as derived from 12 years of *Terra* and over 9 years of *Aqua* data.

II. MODIS Cloud Products

Terra and *Aqua* MODIS data are processed at Goddard Space Flight Center into 5-minute granules (~2000 km in length along the orbital track and 2330 km across track), producing some 244 granules (or files) per day per data product. The atmosphere products, including the cloud mask and cloud product, are described in some detail by King *et al.* [12] and Platnick *et al.* [37]. There have been a number of reprocessings (referred to as "collections") due to improved understanding of instrument calibration and trends, an-

cillary datasets, physical understanding, and algorithm enhancements. This study uses Collection 5.1 data products, which commenced in November 2008, and which were reprocessed throughout the entire data record in a consistent manner. Minor differences between Collection 5.1 and earlier collections, are described below, as appropriate.

A. Cloud Mask

The cloud mask (archived filenames MOD35 for *Terra* and MYD35 for *Aqua*) classifies each pixel as either *confident clear*, *probably clear*, *probably cloudy*, or *cloudy*. The cloud mask consists of 48 bits of output that include information on individual cloud test results, the processing path, ancillary information (e.g., land/sea tag), and additional information (e.g., thin cirrus detected, heavy aerosol). The cloud mask algorithm [1] [6] uses a series of threshold tests applied to as many as 22 of the 36 MODIS bands to identify the presence of clouds in the instrument field-of-view. The specific tests executed are a function of surface type, including land, water, snow/ice, desert, and coastal, and are different during the day and night. Each cloud detection test returns a confidence level that the pixel is clear, ranging in value from 1 (high confidence clear) to 0 (low confidence clear). Tests capable of detecting similar cloud conditions are grouped together and a minimum confidence is determined for each group. The final cloud mask is then determined from the product of the results from each group. This approach is clear-sky conservative in the sense that if any test is highly confident that the scene is cloudy, the final clear sky confidence is 0. The first 2 bits of the cloud mask provide a summary adequate for many processing applications, but the processing path and choices made in arriving at this conclusion are often used in subsequent Level-2 cloud processing algorithms.

The vast majority of improvements over the earlier (Collection 4) cloud mask algorithm concern nighttime scenes, including polar night, and sunglint areas over the ocean during the day. Additional improvements have been incorporated for daytime snow conditions. Furthermore, comparisons with ground-based, aircraft, and spaceborne lidar has

demonstrated the MODIS cloud mask is capable of detecting clouds having a visible optical thickness of 0.4 or greater [2]. Holz *et al.* [8] further showed that the Cloud-Aerosol Lidar with Orthogonal Polarization (CALIOP) 1-km cloud layer product agrees with the MODIS 1-km cloud mask in 87% of cloud conditions, with the best agreement being for nonpolar daytime conditions.

B. Cloud Top Properties

The cloud product (archived filenames MOD06 for *Terra* and MYD06 for *Aqua*) combines thermal infrared and shortwave reflectance techniques to determine the physical, radiative, and microphysical properties of clouds [37] [12]. The cloud top properties (cloud top pressure, temperature, and effective cloud amount) are produced for the cloudy portion of the 5 × 5 pixel arrays wherein the cloud pixels (identified by the probably cloudy and cloudy bits of the cloud mask) are averaged to reduce noise. Unlike the CERES implementation of cloud top properties from MODIS [22], [23], which relies on a minimum set of five MODIS bands in order to be consistent with VIRS capability on TRMM, the MODIS science team utilizes an extended suite of bands, in particular bands in the CO_2 absorption region from 13.3 to 14.2 μm. These so-called CO_2-slicing bands have a long history of use in identifying cloud top pressure for high clouds due to the opacity of CO_2, a uniformly mixed (but temporally changing) gas in the Earth's atmosphere [18], [11], [48]. They are, however, less capable for determining cloud top pressure (or altitude) for low boundary-layer clouds. In MODIS, the CO_2-slicing bands are supplemented with an infrared window band at 11 μm for optically thicker and lower-level clouds.

Menzel *et al.* [20] describe the testing and validation of the MODIS cloud top properties algorithm implemented in Collection 5.1. This algorithm utilizes a 'top-down' approach in which it searches for the cloud top pressure from the top of the atmosphere downward, and utilizes somewhat different CO_2-slicing band combinations for *Terra* and

Aqua, due to enhanced noise problems in band 34 (13.65 μm) of *Terra*. Due to an apparent cold scene calibration error, there is a radiance adjustment required due to an apparent spectral response function change, and a shift of some 1 cm^{-1} is sufficient to bring the Atmospheric Infrared Spectrometer (AIRS) and MODIS CO_2-slicing bands into closer agreement (on *Aqua*). With all of these changes, described in some detail in [20], MODIS cloud top pressures are generally within 50 hPa of independent lidar determinations for single-layer clouds, increasing to much larger errors, or systematic biases, for marine boundary layer clouds in which there is a temperature inversion. The cloud top pressure in Collection 5.1 is provided every 5 km globally (day and night).

C. Cloud Thermodynamic Phase

An important component of the MODIS cloud product is the thermodynamic phase of the cloud, which is used in subsequent processing of cloud optical and microphysical properties. The retrieval phase algorithm (SDS name Cloud_Phase_Optical_Properties) as currently implemented in Collection 5.1 makes extensive use of many of the individual tests in the cloud mask product for a given pixel, supplemented by shortwave infrared ratio thresholds that depend on the underlying surface type. The algorithm uses different short wavelength (non-absorbing) bands to define the shortwave infrared ratio, and *Terra* uses both a ratio of reflectance at 2.1 μm as well as 1.6 μm to a short wavelength band in this SWIR threshold part of the test, whereas *Aqua* uses only 2.1 μm because the 1.6 μm band has many dead detectors on *Aqua*. At the end of the logic tree, if the cloud top temperature is found to be greater than 273 K, the phase of the cloud is switched to liquid water if it had previously been estimated to be ice. A detailed flowchart and explanation of this algorithm can be found in [13] as applied to MODIS and the MODIS Airborne Simulator over ocean, and [15] for a full set of flowcharts for *Terra* and *Aqua* for all ecosystems. By and large, these updates to the thermodynamic phase algorithm have resulted in an almost complete determination of thermodynamic phase for all cloudy pixels during

the daytime, in contrast to the thermodynamic phase algorithm implemented in earlier (Collection 4) versions [37], wherein there were a large number of clouds of undetermined phase (which were subsequently processed as if they were liquid water).

D. Cloud Optical and Microphysical Properties

The cloud product includes the determination of cloud optical thickness, effective radius, and integrated water content of both liquid water and ice clouds for pixels identified as probably cloudy or cloudy by the cloud mask during the daytime portions of each orbit. The basic physical principle behind the simultaneous retrieval of cloud optical thickness and effective radius is the bispectral solar reflectance method first described by Nakajima and King [28]. Implementing this method on a global basis and under all cloud conditions has resulted in a number of practical enhancements and significant features. Among the more significant updates from previous versions (Collection 4) [37], [12] are: (i) new ice crystal size/habit distribution models and the corresponding ice reflectance library calculations [4], (ii) a clear sky restoral algorithm that attempts to identify pixels that are poor retrieval candidates due to sunglint, edges of clouds, heavy dust contamination, or spatially variable (partly cloudy) pixels, in which case these 'cloudy' pixels are *restored* to clear sky and no cloud optical property retrievals are attempted [33, 53], (iii) improved snow-free surface albedo maps [25], [27], and (iv) spectral sea ice and snow-covered land surface albedo characteristics by ecosystem [26].

In addition, a shortwave infrared technique for retrieving cloud optical thickness and effective radius over snow and ice surfaces [36] was implemented, though this appears to work better for liquid water clouds than for ice clouds over snow [14]. The CERES team has also implemented this approach for retrieving cloud optical properties in Polar Regions using MODIS data [22]. Additional subtle and less obvious changes from Collection 4 are changing the solar zenith angle threshold for 'daytime' observations to 81.4°, bringing the cloud optical property retrieval in line with the cloud mask determination of

cloud cover using daylight bands. We also modified the cloud water path formula for ice clouds, recognizing that the density of ice is closer to 0.93 g cm^{-3} than 1 g m^{-3} (used for liquid water clouds). There are a number of additional modifications that are important for in-depth studies of cloud optical properties on a granule basis, including a new multi-layer cloud flag [45], changes to the solar spectral irradiance used in the 3.7 μm band to convert radiance to reflectance, and the addition of pixel-level uncertainties. King *et al.* [15] summarize all of these changes in Collection 5. Collection 5.1 incorporated a code correction that affected cloud optical thickness retrievals over land only, and the entire *Terra* and *Aqua* datasets have been reprocessed with all code corrections identified.

III. Level-3 Cloud Products

The MODIS atmosphere Level-3 products (designated MOD08 for *Terra* and MYD08 for *Aqua*) are available for different time intervals (daily, eight-day, and monthly) and are sorted into 1° × 1° cells on an equal-angle global grid (180 × 360 cells). Each product is derived from four Level-2 atmosphere data products: aerosol, water vapor, cloud, and atmospheric profiles [12], and contain hundreds of Science Data Sets (SDSs), or statistics. SDSs derived from the cloud mask-related data are read from the cloud product MOD06/MYD06, where the first 8 bits of the cloud mask are replicated. Statistics that are included in each file may include (i) scalar statistics (mean, standard deviation, minimum, maximum), (ii) QA (quality assurance)-weighted statistics (mean and standard deviation), (iii) parameters of normal and log-normal distributions, (iv) fraction of pixels that satisfy some condition (e.g., cloudy, clear, liquid water, ice), (v) uncertainty in the mean for selected cloud parameters, and (vi) histograms of the confidence placed in each measurement. They also include marginal probability density functions and joint probability density functions of various cloud parameters.

A. Daily Gridded Products

The Collection 5.1 Level-3 MODIS atmosphere daily global product contains nearly 700 statistical SDSs that are derived from 106 scientific parameters read from four Level-2 MODIS atmosphere products [10]. Among these, 354 SDSs are derived from the cloud product. The daily Level-3 product contains statistics computed for a 24-hour time interval from 0000 to 2400 UTC, which may result in a granule of Level-2 data being split between days based on the UTC day of acquisition. All Level-2 geophysical parameters that are input to the Level-3 daily product are sampled every 5 km or 10 km (depending on input data product), thus reducing the number of pixels that are aggregated in the gridded product. For all cloud products, which were generated at either 1 km or 5 km spatial resolution, a 5 km sampling was used. Thus, for a 1° × 1° grid box at the equator, a maximum of 484 pixels were used (out of a potential total of 12,321 pixels for 1 km cloud optical properties or cloud mask), reducing to fewer pixels at higher latitudes where a 1° × 1° box is geometrically smaller in area than at the equator. A software modification was introduced in Collection 5 (and 5.1) that offset slightly the Level-2 data point that was sampled. This was in order to avoid Level-2 data from MODIS detectors that were known to be dead (especially on *Aqua*) from being subsampled in the Level-3 product. This avoided completely missing (or fill values) in the Level-3 daily cloud properties.

An additional feature of the Level-3 daily product is that there are 16 overlapping orbits near 82° latitude (each one roughly 98 minutes apart) that cause "time averaging" to occur for daily statistics computed poleward of about 77° (that is, they tend to be daily average statistics), in contrast to those at mid-latitudes (that typically can be pinned down to within 20 minutes of a MODIS instrument overpass).

All Level-3 products (daily, eight-day, and monthly) make use of aggregation and QA weighting capabilities. Aggregation routines include the ability to separate Level-2 input pixel information into various scientifically relevant categories such as liquid water clouds

only, ice clouds only, daytime only, nighttime only, clear sky only, etc. These routines utilize L2 "Runtime QA Flags" that are designed to convey information on retrieval processing path, input data source, scene characteristics, and the estimated quality of the physical parameters retrieved. In Level-3, these statistics are noted by a suffix to the SDS name (_Liquid, _Ice, etc.).

QA weighting refers to the ability to weight more heavily what are expected to be more reliable Level-2 input pixels in the computation of Level-3 statistics. There are four levels of "reliability" or "confidence" set by the Level-2 QA confidence flags for some, but not all, Level-2 products [9]. These four levels are: no confidence or fill (QA = 0), marginal confidence (QA = 1), good confidence (QA = 2), or very good confidence (QA = 3). QA weighted statistics always have the identifying string "QA" somewhere in the SDS name (for example: "QA_Mean"). QA weighted statistics are computed by weighting all Level-2 pixels by their QA confidence as follows

$$\text{QA-weighted mean} = \sum_i Q_i d_i \Big/ \sum_i Q_i , \tag{1}$$

where the weights Q_i are the QA values (0, 1, 2, or 3) and d_i are the geophysical parameters (e.g., cloud optical thickness) for the ith pixel in the grid cell. All non-fill QA = 0 pixels are included in regular statistics (mean, standard deviation), but they are screened (removed) from the QA-weighted statistics.

Of particular value in the Level-3 daily file is the marginal histogram that contains pixel counts showing the distribution of non-fill Level-2 geophysical parameters that went into the computation of the Level-3 statistics such as mean and standard deviation. This histogram can readily be converted into a marginal probability density function if one takes account of the various widths of the bin boundaries in the histogram. In many cases, the distribution of geophysical parameters is highly non-Gaussian, and thus the distribution of retrieved values provides information that is often distorted by only looking at

the mean value. For selected cloud properties, the Level-3 file also contains a joint histogram (or equivalently joint probability density function) between selected cloud parameters for each grid cell.

B. Eight-Day and Monthly Gridded Products

The Collection 5.1 Level-3 MODIS atmosphere eight-day and monthly global products contain over 900 statistical SDSs that are derived from statistics within the daily L3 global product only [10]. Among these, 509 SDSs are cloud properties. In order to generate multiday Level-3 products, the only inputs that are used are the Level-3 daily files, and there are two different multiday weighting schemes used for the cloud products: (i) unweighted (a simple time-averaged mean), and (ii) pixel-count weighted (a count-averaged mean). An unweighted statistic is computed by taking an average of all Level-3 daily values for a given 1° × 1° grid cell and for the time period in question. This is the multiday weighting scheme used for the cloud fraction and all cloud top properties. The SDS name for these files contains a suffix such as _Mean_Mean that denotes 'mean of the daily mean.' Hubanks *et al.* [10] describe this and all other multiday simple mean SDSs.

For cloud optical properties, such as cloud optical thickness, effective radius, and water content, a pixel-count weighting is employed for multiday Level-3 grid cell characteristics. A pixel count of all non-fill Level-2 pixel data are read in and used to compute statistics at Level-3. This is computed by simply summing the daily pixel count SDS.

The Level-3 eight-day and monthly files also contain marginal histograms that are computed by simply summing the daily counts in each histogram bin. A confidence histogram is also provided that provides the number of pixels with various levels of QA that went into the computation of Level-3 statistics within the grid cell. For selected cloud properties, the Level-3 eight-day and monthly files also contain joint probability density functions (or joint histograms) between selected cloud parameters for each grid cell. There are 23 joint histograms defined in the Level-3 atmosphere product for Collection

5.1, all of which are derived from the cloud product. These joint histograms, which are summarized in Hubanks *et al.* [10], are stored as 4-dimensional arrays (latitude, longitude, parameter1bins, parameter2bins) and thus constitute a large fraction of the file size in MOD08 for *Terra* and MYD08 for *Aqua*.

IV. Global-Level Cloud Properties

A. Cloud Fraction

Fig. 1 shows the Collection 5.1 monthly mean cloud fraction (amount) as derived by the MODIS cloud mask for July 2006 from *Aqua*. As different spectral bands are used to detect clouds during the daytime and nighttime, it is valuable to separate the cloud fraction derived during the daytime (Fig. 1a) and nighttime (Fig. 1b). These results, as illustrated here, show a remarkably similar cloud amount detected during the daytime and nighttime. Ackerman *et al.* [2] have demonstrated, through comparison with ground-based, airborne, and spaceborne lidar, that the cloud mask detects clouds down to an optical thickness $\tau_c \sim 0.4$. This sensitivity is partially the result of the relatively high spatial resolution and broad spectral range available in MODIS, but very thin clouds below this threshold are simply too difficult to detect using passive remote sensing. The global cloud fraction detected by MODIS is approximately 0.68, somewhat smaller than that detected by CALIOP on the CALIPSO (Cloud-Aerosol Lidar and Infrared Pathfinder Satellite Observation) satellite, which has a detection limit down to $\tau_c \sim 0.1$ [46]. Similarly, Wang and Dessler [44] find that the Geoscience Laser Altimeter System (GLAS) on ICESat (Ice, Cloud, and Land Elevation Satellite) retrieves a global cloud fraction of 0.75, similar to the conclusions of Ackerman *et al.* [2] who report that GLAS detects ~5% more clouds than MODIS.

The large-scale patterns illustrated in Fig. 1 are similar to other satellite datasets of cloud amount [41], [48], [24], [33], with generally high cloud amount in the intertropical convergence zone, "roaring 40s" of the southern hemisphere, western tropical Pacific,

and the marine stratocumulus regions, with correspondingly low cloud amounts over the subtropical gyres of the oceans, deserts, Greenland, and Antarctica. Figure 1a does not show daytime cloud amount over Antarctica because there is polar darkness and no solar illumination in July, but the nighttime cloud fraction is low over Antarctica, as also noted by Wu *et al.* [46]) from spaceborne lidar observations.

Fig. 2 shows the seasonal mean daytime cloud fraction from *Terra* and *Aqua* based on averages over multiple years. *Terra*, shown in the left hand column, is based on Collection 5.1 retrievals from 2000-2011, and the right-hand column shows *Aqua* results from 2002-2011. These multiyear averages show similar seasonal distributions, with the intertropical convergence zone systematically moving in latitude as the sun moves throughout the year, reaching its highest northern latitude in the boreal summer (June-August, Fig. 2c) and its lowest southern latitude in the winter (December-February, Fig. 2a). Throughout the year, Greenland and Antarctica exhibit very low cloudiness, and there is only minor seasonal variation in the frequency of clouds in the marine stratocumulus regions off Angola and Namibia in Africa and Ecuador and Peru in South America. Of particular note is that the peak frequency of marine stratocumulus clouds in the southern Hemisphere occurs between June and November, whereas California stratocumulus peaks in June-August, and thus these cloud systems are not 6 months out of phase as one might expect (also see Fig. 9).

One of the advantages of MODIS is that there are two spacecraft carrying the MODIS sensor. A visual comparison of the *Terra* and *Aqua* cloud fractions shows that there are generally more clouds over land from *Aqua* (afternoon), whereas the oceans are cloudier at the time of the *Terra* overpass (morning). Fig. 3 illustrates this diurnal variation in cloud fraction more explicitly, where each figure shows *Aqua* minus *Terra* (i.e., 1330 minus 1030 local time) for a different three-month season and for a nine-year period (September 2002-August 2011). In all instances, the marine stratocumulus areas show

less (and generally optically thinner, not shown) clouds in the afternoon (*Aqua*) than the morning (*Terra*), leading to blue colors in Figs. 3a-d. The diurnal effect is greatest in the Peruvian and Angolan stratocumulus regions in and September-February (Fig. 3d, a) than in March-August (Figs. 3b, c), as also noted by Ackerman *et al.* [2]. During all seasons, the land exhibits more cloudiness in the afternoon than the morning, by up to 20%, as also observed by Meskhidze *et al.* [21], Minnis et al. [24], and Ackerman *et al.* [2].

Fig. 4 shows the zonal mean daytime cloud fraction for both *Terra* and *Aqua*, separated by ocean and land, for all four seasons. These results are based on multi-year averages for *Terra* (2000-2011) and *Aqua* (2002-2011). In all seasons and most latitudes, the cloud fraction is greater over ocean than land, and is especially high in the southern oceans, as expected by examination of Fig. 2. The location of the ITCZ (intertropical convergence zone) is clearly seen to move north and south of the equator, depending on season, with correspondingly reduced cloud fraction in the subtropical latitudes from about 15°-30° of both hemispheres. *Aqua* again has somewhat more cloudiness over land than *Terra* for all seasons, in contrast to the oceans where there is generally more cloudiness at the time of the *Terra* overpass (1030 local time) than *Aqua* (1330 local time).

There is typically more cloudiness at night than during the day, for both *Terra* and *Aqua* (not shown), though the differences are generally less than 0.10. Holz *et al.* [8] compared the *Aqua*/MODIS cloud fraction for both day and night with corresponding observations from CALIOP, and found that the cloud detection from MODIS and CALIOP agreed more than 87% of the time, where most of the discrepancies were largely associated with the optically thin clouds ($\tau_c < 0.4$) that were undetected by MODIS but which were readily observed by CALIOP.

Fig. 5 shows a time series of the global mean daytime cloud fraction from *Terra* (dashed) and *Aqua* (solid) for land, ocean, and combined (land and ocean) from the beginning of the time series for each spacecraft. It is again readily apparent that there is more

cloudiness over land in the afternoon (*Aqua*) than during the morning (*Terra*), and that oceans are generally much cloudier than the land. Averaged over both land and ocean and over the entire globe, however, there is very little difference in overall cloud fraction between the morning and afternoon. There is a noticeable seasonal cycle over land, but a much reduced seasonal cycle over ocean. The overall global cloudiness as determined by MODIS is roughly 67% since the very thinnest (subvisible) clouds go undetected in passive remote sensing. What is perhaps more surprising is that there is no noticeable signal in the time series associated with El Niño or La Niña events during this period, showing an overall robustness and stability in the overall global cloud cover, though the spatial distribution does change in response to these natural climatic events.

All cloud fraction and subsequent cloud property retrievals are understandably affected by the view zenith angle of the observations. Maddux *et al.* [17] have shown that the cloud fraction is noticeably smaller for nadir observations than for observations at a slant-viewing angle. This arises in part because the spatial resolution grows from nadir to the edge of scan, which leads to more partially-filled fields of view containing some clouds. The level-3 results described in this paper are produced routinely and take advantage of multiple view zenith angles and multiple satellite overpasses during a specified time interval. As a consequence, they represent a mixture of view zenith angles somewhere between the two extremes of nadir and edge of scan.

B. Cloud Top Properties

Level-3 aggregation of cloud top properties on a global grid consists of cloud top pressure, cloud top temperature, and effective emissivity. Fig. 6 shows the seasonal mean cloud top pressure during the daytime from *Terra* (left-hand column) and *Aqua* (right-hand column), where *Terra* data were averaged from 2000-2011 and *Aqua* data were averaged from 2002-2011. These multiyear averages show well-known cloud characteristics, including high clouds (low cloud top pressures) in the ITCZ, the western tropical Pacific,

India and China, Greenland, Antarctica, and many deserts (with their high thin cirrus clouds). In contrast, low clouds (high cloud top pressure) occur in the central subtropical ocean gyres, southern Indian Ocean, and southern Europe. Since this product is based in part on CO_2 slicing, which is especially sensitive to ice clouds in the upper atmosphere (where $\tau_c > 1$), and in part on thermal emission in the infrared window around 11 μm (for low-level liquid water clouds), it is especially accurate for higher clouds and is less accurate for low-level water clouds, especially over the marine stratocumulus regions that are overlaid with temperature inversions [8]. For optically thin cirrus and mid-level water clouds it is known to be accurate to within 1 km (or 50 hPa), based largely on comparisons with airborne and spaceborne lidar [20]. The results shown in Fig. 6 are multiyear and seasonal averages, but are similar to those reported by Menzel *et al.* [20] based on four years of *Aqua* data.

Fig. 7 shows the zonal mean daytime cloud top pressure for both *Terra* and *Aqua*, separated by ocean and land, for all four seasons. These results are based on multi-year averages for *Terra* (2000-2011) and *Aqua* (2002-2011). In all seasons and most latitudes, the cloud top pressure is lower over land than ocean, reflecting generally deeper convection and higher clouds over land than over the ocean, an observation first reported by Rossow and Lacis [38] based on the Scanning Radiometer (SR) on the NOAA-5 operational polar-orbiting satellite. Clouds are especially high over the northern hemisphere continents between 30° and 50°, and expected by examination of Fig. 6. Because these are daytime results only, the coverage in Polar Regions is restricted to seasons for which sunlight is present, and thus is absent during months of polar darkness. The location of the ITCZ over the ocean is clearly seen to move north and south of the equator, depending on season. *Aqua* and *Terra* have comparable zonal cloud top pressures, with *Aqua* having somewhat higher clouds (lower cloud top pressures) over land due to afternoon deep convection.

With the advent of the multiple wavelengths and high spatial resolution capability of MODIS, the cloud top pressures range to much lower pressures (higher altitude clouds) than ISCCP, which relies primarily on one visible and one thermal infrared window band to determine cloud top pressure. Rossow and Schiffer [40] report annual mean zonal cloud top pressures that are much higher pressure over land (and much closer to Fig. 7 over ocean), as a result of the inadequate sensitivity to high thin clouds in ISCCP that MODIS is able to achieve. Pincus *et al.* [33] also report that MODIS has more high cloud and more low cloud that ISCCP, and less mid-level cloud.

Fig. 8 shows the seasonal mean cloud top temperature during the daytime from *Terra* (left-hand column) and *Aqua* (right-hand column) for the same multi-year time periods as shown in Fig. 6 for cloud top pressure. These multiyear averages show well-known cloud characteristics commensurate with the cloud top pressure expectations, but the cloud top temperature is more accurate than cloud top pressure for low-level boundary level marine stratocumulus, which often exhibit a temperature inversion above cloud top. The coldest cloud tops generally occur over Antarctica and the high clouds in the tropics (ITCZ and the deep convective clouds over the western tropical Pacific and Indian subcontinent. The cold clouds over the Sahara, though infrequent (cf. Fig. 2) are generally high, thin cirrus.

C. Cloud Optical and Microphysical Properties

One of the strengths of MODIS is its ability to retrieve cloud optical thickness and effective radius, and thereby derive integrated water content, for both liquid water and ice clouds. This is accomplished in part by the high spatial resolution and wide wavelength range available on the MODIS sensors. Fig. 9 shows the seasonal mean daytime cloud retrieval fraction of both liquid water clouds, in the left hand column, and ice clouds, in the right hand column, from *Aqua* based on averages from 2002-2011. These results correspond to all clouds for which there are successful cloud optical property retrievals (i.e.,

both optical thickness and effective radius are within the forward model retrieval space), with the sum of the liquid water and ice cloud fractions generally being less than the total cloud fraction identified by the cloud mask (cf. Fig. 2). This is by design, as there was an explicit attempt to remove cloud edges and spatially nonuniform (partly cloudy) pixels from the retrieval of cloud optical properties due to their expected erroneous impact on cloud retrievals using plane-parallel radiative transfer theory. As a result, pixels containing cloud edges and generally most optically thin (and partly cloudy) pixels were removed from the optical properties analysis, with the expectation that the retrieved optical properties better match the cloud radiative models and are therefore more accurate. This algorithm, known as clear sky restoral, is described in some detail in [15] and discussed extensively by Pincus et al. [33] and Zhang and Platnick [53].

These multiyear averages show the seasonal and spatial distribution of well-known cloud regimes, with liquid water clouds, such as marine stratocumulus, occurring frequently off the west coast of the United States, Ecuador, Peru, Namibia, and Angola, with some seasonal movement, and additional altocumulus and cumulus humilus clouds occurring in the north Pacific, summertime Arctic, and Indian subcontinent. Ice clouds are prevalent in the ITCZ, western tropical Pacific, and the southern oceans, as well as the Congo (year round) and the Amazon (wet season only). Though Fig. 9 shows results that apply to the afternoon orbit of *Aqua*, *Terra* has produced quite similar results except that the frequency and extent of the marine stratocumulus clouds over the eastern subtropical oceans is somewhat greater and more extensive in spatial extent in the morning (*Terra* orbit), since these clouds tend to thin out and burn off in the afternoon. Minnis *et al.* [23] report an annual average of liquid water and ice cloud fraction based on the CERES-MODIS algorithm that is similar to Fig. 9 in overall cloud phase characteristics.

Fig. 10 shows the zonal mean daytime cloud retrieval fraction for *Aqua* (2002-2011), separated by ocean and land and thermodynamic phase, for all four seasons. Liquid wa-

ter clouds over the land (Fig. 10a) are the greatest during northern summer in the tropics, primarily associated with the monsoon over the Indian subcontinent (cf. Fig. 9c). In contrast, liquid water clouds over the ocean (Fig. 10b) show the most extensive clouds in the northern and southern subtropics, associated with the marine stratocumulus regimes, and there is modest seasonal variation, as expected from comparison to Fig. 9. Ice clouds are extensive in the tropics for both ocean and land regions, associated with deep convection over land (Fig. 10c) and the ITCZ over ocean (Fig. 10d), with some seasonal variation associated with movement of the ITCZ as the sun moves throughout the year. A secondary maximum in ice cloud occurrence is observed in the Polar Regions during periods of enhanced sunlight in the summer. Comparing Fig. 10 to Fig. 4, one readily sees that the total cloud fraction for liquid water and ice clouds is less than that of the total cloud fraction of possible retrievals, by sometimes as much as 20%, but as previously mentioned, these excluded edge pixels are often the most optically thin and the most prone to erroneous cloud retrievals.

Once the cloud phase has been identified and cloud optical properties derived, one can assess the spatial and temporal distribution of the resulting cloud optical thickness and effective radius. Fig. 11 shows the seasonal mean cloud optical thickness of both liquid water and ice clouds from *Aqua* averaged from 2002-2011. These results clearly show that clouds over land, regardless of whether they are composed of liquid water or ice, are generally much more optically thick than clouds over ocean. Marine stratocumulus clouds typically have $\tau_c \sim 10\text{-}12$, whereas clouds over land often have $\tau_c > 20$. Ice clouds over the tropical ocean associated with the ITCZ have large optical thicknesses associated with their convective core and convergence, as do deep convective clouds over land in the Congo and Amazon, but ice clouds in the southern ocean surrounding Antarctica also exhibit large values of cloud optical thickness, especially between March and August. The western tropical Pacific, which has a large cloud fraction composed primarily of ice

clouds (cf. Fig. 9) has relatively low cloud optical thickness. This is to be expected from the preponderance of cirrus anvil clouds in this region. These findings are similar to the findings of Minnis *et al.* [23], who report multiyear averages of cloud optical thickness based on using five bands of MODIS in the CERES-MODIS Edition-2 algorithm.

Fig. 12 shows the zonal and seasonal mean cloud optical thickness for *Aqua* (2002-2011), separated by ocean and land and thermodynamic phase. As expected from Fig. 11, the optical thickness of both liquid water (Fig. 12a) and ice (Fig. 12c) clouds over land is the greatest during summer, thus moving somewhat with the seasonal movement of the sun. The secondary peak in optical thickness of liquid water clouds over land between 0° and 20° in June-August is associated with the monsoons of the Indian subcontinent. In contrast, ice clouds over the ocean (Fig. 12d) have the largest optical thickness over the southern ocean associated with the roaring 40s, with a secondary peak in the ITCZ that moves north and south in latitude with the season. Liquid water clouds over the ocean (Fig. 12c) exhibit relatively little variation in zonal cloud optical thickness except in the latitudes containing the marine stratocumulus regions of the eastern subtropical oceans. We note that ice cloud retrievals are particularly sensitive to particle shape (habit) assumptions [4, 52].

The effective radius of both liquid water and ice clouds is derived as part of the cloud product using the bispectral solar reflectance method first described by Nakajima and King [28] and discussed in detail by Platnick *et al.* [37]. Although MODIS derives the effective radius (r_e) using 3 separate bands (1.6, 2.1, and 3.7 μm), in combination with a nonabsorbing band used for deriving the cloud optical thickness, the primary band used in global aggregation to Level-3 is the 2.1 μm band. Fig. 13 shows the seasonal mean cloud effective radius of both liquid water and ice clouds from *Aqua* averaged from 2002-2011. These results show that liquid water clouds over ocean have larger droplet radii than corresponding clouds over land, as first noted by Han *et al.* [7], who used

NOAA/AVHRR data for selected months over two years. Although [7] utilized 3.7 μm to derive cloud effective radius, rather than 2.1 μm, as used here, they found results in qualitative agreement with Fig. 13, from which they concluded that liquid water clouds over land have smaller droplet sizes than over ocean, largely as a result of having more aerosol particles over land that serve as cloud condensation nuclei and thus make clouds having a larger number of cloud drops that are necessarily smaller in size. They also found that liquid water clouds over the southern oceans tended to be somewhat larger than those over the northern oceans. The CERES-MODIS Edition-2 algorithm [22], which relies only on 3.7 μm, results in seasonal distributions of cloud effective radius for liquid water clouds similar in overall features to those shown in Fig. 13 (left hand column), as illustrated in Minnis *et al.* [23].

The results in Fig. 13 show that the cloud droplets over ocean are smallest in marine stratocumulus regions that have large fractions of liquid water clouds (cf. Fig. 9). Over the open ocean, the effective radius of liquid water clouds is considerably larger than that found in coastal stratocumulus regions, but these clouds are also more likely to be broken and optically thinner (cf. Fig. 11). A number of studies have examined the effective radius of liquid water clouds from MODIS derived using the 2.1 μm standard retrieval, and noted how much larger these cloud droplet retrievals can be than those derived using the 3.7 μm band. Nakajima *et al.* [31], [32] used collocated CloudSat Cloud Precipitation Radar (CPR) and Aqua/MODIS observations to show that small cloud drops at the top of liquid water clouds lead to smaller 3.7 μm retrievals than 2.1 μm, which is sensitive to cloud droplets somewhat lower in the cloud, as pointed out by Platnick [34]. In contrast, the larger 2.1 μm-retrieved cloud drops deep within the cloud are sometimes affected by the presence of large drizzle droplets that are insensitive to the 3.7 μm retrieval. Zhang and Platnick [53] further studied the influences of different shortwave infrared retrievals on cloud effective radius of liquid water clouds, and found that 2.1 μm retrievals are far more

sensitive to cloud inhomogeneity and 3-D radiative effects, and can lead to substantial differences between 2.1 and 3.7 μm retrievals of effective radius when r_e (2.1 μm) > 15 μm and/or the 250m sub-pixel spatial heterogeneity is high. This is, in part, the reason that the MODIS Collection 5.1 cloud optical properties algorithm explicitly removed edge pixels from the retrievals, expecting that the retrieved results were less consistent with radiative transfer models used in the analysis. While this did result in a reduction in optical thickness, effective radius histograms did not typically change in a manner that led to significant reductions in mean size [53].

The effective radius of ice clouds shown in Fig 13 (right hand column) shows far less spatial variability than the effective radius of liquid water clouds (left hand column), but there is still a tendency for ice clouds to have somewhat larger particles over ocean than over the land, especially in the tropical latitudes. Ice crystals also tend to be smaller at the top of deep convective clouds. The range of sizes of ice crystals in global clouds is generally much smaller than the range of sizes of liquid water droplets in clouds.

Fig. 14 shows the zonal and seasonal mean cloud effective radius for *Aqua* (2002-2011), separated by ocean and land and thermodynamic phase. As expected from Fig. 13, the effective radius of liquid water clouds over land (Fig. 14a) exhibits very little seasonal or latitudinal variation, except during the convective seasons of the southern subtropics. In contrast, the effective radius of liquid water clouds over ocean (Fig. 12b) exhibits some seasonal variation, with the largest effective radius occurring in the equatorial tropics with a secondary peak in the midlatitudes during the winter of the Southern Hemisphere (June-August). Ice clouds over land (Fig. 14c) show very little seasonal variation except at high latitudes, with small values in summer and large values in winter and spring in the Northern Hemisphere, and in the subtropics around 20°S and 20°N where the cloud fraction over land is generally small. Over ocean, the effective radius of ice clouds is generally greatest in the tropics (Fig. 14d) with declining values at high latitudes

of both hemispheres. Minnis *et al.* [23] show zonal and seasonal mean results for the effective radius of liquid water clouds over the ocean for four years of *Terra* data, based on the CERES-MODIS Edition-2 algorithm. These results, which are roughly analogous to Fig. 14b, show very similar seasonal variations to those reported here.

D. Histograms and Joint Histogram

In addition to scalar statistics (mean, maximum, minimum, standard deviation), the Level-3 products also contain histograms of the quantity within each grid box (1° x 1°) for a specified time period (daily, eight-day, or monthly). Fig. 15a shows comparisons of the marginal probability density function of global cloud optical thickness for liquid water clouds from both *Terra* and *Aqua* for July 2006, with Fig. 15b showing the corresponding results for all ice clouds. Note that in both cases, the histograms of cloud optical thickness are highly non-Gaussian, with the mode optical thickness being substantially less than the mean. The discrete values of optical thickness intervals on the abscissa axes represent the discretization in optical thickness in the Level-3 histogram product for Collection 5.1, representing a higher resolution discretization for liquid water clouds than for ice clouds. The tendency for the peak (mode) of the cloud optical thickness histograms to be around 3-4 for liquid water clouds and 2-3 for ice clouds also represents the effect of our clear sky restoral algorithm in which the optically thinnest, and least accurate, edge pixels have been eliminated from our analysis of cloud optical properties. There is little difference in the global distribution of cloud optical thickness between *Terra* and *Aqua*, but ice clouds over land are somewhat more optically thick than ice clouds over ocean. Overall, cloud optical thickness $\tau_c > 15$ occurs for ~35% of all liquid water clouds.

Fig. 15c shows the probability density function of effective radius for global liquid water clouds and Fig. 15d the corresponding probability density function for all ice clouds for both satellites from July 2006. Although the effective radius of ice clouds is very similar over both land and ocean and Terra and Aqua, the results over ocean (Fig. 15c) show

the expected bias between ocean and land, where the effective radius of liquid clouds over the ocean is larger than that over land. There is very little difference in these optical properties between *Terra* and *Aqua*, although the effective radius of liquid water clouds is again clearly non-Gaussian, with the mode of the distribution generally much smaller than the mean. Suzuki *et al.* [43] also show histograms of cloud optical thickness and effective radius for liquid water clouds and find results quite similar to those in Figs. 15a and 15c. They also show the probability density function of effective radius retrieved using the 3.7 μm band, and show, once again, that these values are generally smaller than the corresponding results obtained using the 2.1 μm band. This is said to be due to the physics associated with the vertical distribution of effective radius, especially for clouds with droplets large enough for coalescence (and hence drizzle) and for edge pixels associated with 3D radiative properties. This is not due to algorithm deficiencies, as demonstrated by Zhang and Platnick [53], and is an additional source of information on cloud microphysical characteristics.

In addition to the simple statistics and histograms of some cloud parameters, the Level-3 product contains 23 joint histograms of selected variables, as discussed by Hubanks *et al.* [10]. Fig. 16 shows a joint histogram of cloud optical thickness and effective radius for liquid water clouds over ocean for a region off southern California bounded by 32°-40°N and 117°-125°W for the month of July 2006, where Fig. 16a is for *Terra* and Fig. 16b is for *Aqua*. For this region of widespread boundary-layer stratocumulus, the cloud optical thickness and effective radius are positively correlated, such that clouds having larger optical thickness also have larger effective radius. The bin boundaries of the aggregated histogram are clearly seen in this figure. Nakajima *et al.* [29] studied this same region of marine stratocumulus from airborne observations and found some days in which τ_c and r_e were positively correlated and other days for which they were negatively correlated. Fig. 16 represents a monthly average and thus reflects a mixture of meteoro-

logical conditions such that it is not feasible to draw any cause and effect conclusions from such relationships. Joint histograms such as these nevertheless represent the dominant statistical properties of cloud optical properties for a given region and time period, and are thus useful properties with which to compare to general circulation models.

As a comparison to the marine stratocumulus clouds over ocean off California, we have also extracted the joint histogram of liquid water clouds over ocean for a region off Peru bounded by 12°-24°N and 68°-80°W for the month of August 2006, where Fig. 16c is for *Terra* and Fig. 16d is for *Aqua*. As in the case of California stratocumulus, this region also shows that the cloud optical thickness and effective radius are positively correlated, such that clouds having larger optical thickness also have larger effective radius. In both California and Peruvian stratocumulus, the joint probability density function is normalized such that a summation over the probability density function and the area of each grid cell sums up to unity. Hence, the actual magnitude of the joint probability density values varies for each panel, but is unimportant to appreciate the relative probability in these joint histograms.

Of great interest is the two dimensional histogram of cloud top pressure and cloud optical thickness, first pioneered by ISCCP [39]. In Collection 5 (and 5.1), we have added an ISCCP-like joint histogram using the same cloud optical thickness and cloud top pressure levels defined by ISCCP. Since ISCCP does not have the capability of distinguishing liquid water from ice clouds, we have produced these joint histograms (for every 1° × 1° grid cell) for all clouds for which we have successful cloud optical property retrievals. Fig. 17a shows one such joint ISCCP-like histogram of cloud optical thickness and cloud top pressure derived from *Terra* data between 50°N and 50°S for August 2001. The most frequent clouds occur between an optical thickness of 3.6 and 23 and between cloud top pressures of 680 and 800 hPa. ISCCP classifies these clouds as stratus clouds. Using the full capability of MODIS, however, we are able to discriminate both liquid wa-

ter and ice clouds and to resolve the cloud optical thickness and effective radius at much finer discretization. Fig. 17b shows a joint histogram of cloud top pressure and cloud optical thickness for liquid water clouds in the same latitude band and month as Fig. 17a, with Fig. 17c showing a corresponding joint histogram of all ice clouds identified in this latitude band. Fig. 17b shows that the greatest frequency of low-level water clouds occur between 700 and 800 hPa with an optical thickness between 10 and 15, again primarily stratus clouds in nature. In contrast, the ice clouds identified by MODIS occur largely in the upper atmosphere with a peak concentration between 150 and 250 hPa, and with an optical thickness between 2.5 and 5.

Figs. 16 and 17 demonstrate just four of the joint histograms available in Collection 5.1, with others involving optical thickness and effective radius of single layer clouds (of each phase), optical thickness and effective radius using the 1.6/2.1 μm algorithm [36], [14], cloud top temperature, effective emissivity, and cloud phase infrared.

IV. Summary and Conclusions

Prior to the launch of MODIS on *Terra* in 1999, global cloud properties were largely determined either from (i) the AVHRR sensor onboard the NOAA operational satellites, which contained only 5 spectral bands with relatively wide spectral bandwidth, a single microphysical band at 3.7 μm (or 1.6 μm starting with NOAA-15), global area coverage with 4 × 1 km pixels, no solar reflectance calibration, and no orbit control of the spacecraft, (ii) geosynchronous satellites using one visible and one infrared band from multiple spacecraft that had to be 'intercalibrated' [39], or (iii) infrared sounders that could take advantage of CO_2 slicing to determine cloud fraction and cloud top pressure, but which had a spatial resolution of 20 km [47], [48], [49]. The MODIS sensor contains 36 spectral bands from 0.41 to 14.2 μm, including 3 shortwave infrared bands capable of determining microphysical properties, with all bands at 1 km spatial resolution or better, and has considerable onboard calibration capability in the shortwave as well as thermal infra-

red. Furthermore, the *Terra* and *Aqua* orbits are controlled to within ±1 min, and data are freely and publically available.

The MODIS cloud mask and cloud properties have undergone considerable enhancement in Collection 5 (and 5.1), and these cloud properties are quite stable and reliable, thus enabling over 10 years of global cloud properties to be derived from both *Terra* and *Aqua*. With *Terra* flying in a 10:30 am descending orbit and *Aqua* flying in a 1:30 pm ascending sun-synchronous polar orbit, and with both producing the same data products, we are able to study the diurnal variability of cloud properties over an extended period of time.

MODIS finds the cloud fraction, as derived by the cloud mask, is nearly identical during the day and night, with only modest diurnal variation. Globally, the cloud fraction derived by the MODIS cloud mask is ~67%, with somewhat more clouds over land during the afternoon and less clouds over ocean in the afternoon, with very little difference in global cloud cover between *Terra* and *Aqua*. Overall, cloud fraction over land is ~55%, with a distinctive seasonal cycle, whereas the ocean cloudiness is much higher, around 72%, with much reduced seasonal variation. Overall, there is no global basis for clear-sky observations in the afternoon versus the morning, though these conclusions depend heavily on one's interest in land vs. ocean applications. ISCCP also finds the global cloud fraction ~67%, as discussed by Pincus *et al.* [33], but the cloud fraction is itself a poorly defined quantity, depending on the field of view, radiometric sensitivity, and spectral bands used to derive them. MODIS is able to detect clouds down to a cloud optical thickness of ~0.04, but sometimes clouds are detected that are in fact heavy aerosol or sun glint, so much care must be taken in further applications that depend on these results.

Cloud top pressure and temperature are determined using a combination of the high spatial resolution CO_2 slicing bands in the 15 μm absorption band for high thin clouds and the 11 μm thermal emission band from lower level boundary layer clouds. Cloud top

pressure and temperature have distinct spatial and temporal patterns, and clearly reflect our understanding of global cloud distribution. Based on comparisons with airborne and space-based lidar, the cloud top altitude of upper layer clouds retrieved by MODIS has been shown to be within 1 km (or 50 hPa), but Collection 5.1 has more consistent biases in cloud top pressure for low-level boundary layer clouds, generally placing these clouds at too low a pressure (or too high an altitude) due to the persistent temperature inversions found in marine stratocumulus regions of the globe [8]. Cloud top temperature is retrieved quite accurately in all such situations, however.

The advent of the well-calibrated shortwave infrared bands on MODIS allows the separate determination of cloud optical thickness and effective radius for both liquid water and ice clouds. In Collection 5.1 all retrievals are attempted following the cloud mask, but after implementing additional tests to eliminate partially cloudy and edge pixels, known as clear-sky restoral, and hence the total cloud fraction from which the cloud optical property retrievals are reported is close to 50%, rather than 67%. These cloud optical property results generally apply to clouds of optical thickness $\tau_c > 1.3$, as noted by Pincus *et al.* [33]. We have presented the spatial and temporal distribution of cloud optical properties as well as the zonal variation, which is valuable in assessing the large spatial variation not achievable from periodic airborne field campaigns. The cloud effective radius of liquid water clouds is clearly larger over ocean than land, reflecting the variation in hydroscopic aerosol concentrations that provide cloud condensation nuclei necessary for cloud formation. We also find the effective radius to be larger in the southern hemisphere than the northern hemisphere, again reflecting differences in sources of cloud condensation nuclei.

The mean cloud properties shown in this and other studies must be understood in the context of the probability density function of these properties, and clouds often have a distribution of both optical thickness and effective radius that are non-Gaussian, such that

the mean values of τ_c and r_e are larger than the mode or median values of these parameters. MODIS also permits the examination of many different joint products, such as cloud top pressure and optical thickness, which enable a much greater understanding of the distributions of real clouds in the real atmosphere. We have illustrated several different joint probability density functions (or joint histograms) that illustrate the variation in cloud properties over a one-month time period.

All data produced by the algorithms described in this paper are available from the MODIS Level 1 and Atmosphere Archive and Distribution System (LAADS) search utility (ladsweb.nascom.nasa.gov/data/search.html) or through the LAADS ftp site (ladsweb.nascom.nasa.gov/data/ftp_site.html). Also available from LAADS is a small subset of the Level-3 data sets that match the output of the MODIS cloud simulator that is part of the COSP (CFMIP Observation Simulator Package) software suite [33]; these data are in the NetCDF format and include the CF (climate and forecast) metadata convention. Browse imagery of all Level-1B true color and Level-3 data products are available from the MODIS atmosphere web site at modis-atmos.gsfc.nasa.gov. In addition, this site contains (i) software tools for locating granules, providing spatial subsetting, and visualizing various scientific data sets, (ii) extensive references and descriptions of the algorithms used to process the data, (iii) descriptions of all changes that have been implemented in various Collections, (iv) calendars of data availability, and (v) data issues, where they occur.

ACKNOWLEDGMENTS

The research reported in this article was supported by NASA through the MODIS Science Team. MDK was supported by NASA Grant NNX11AF28G to the University of Colorado and WPM and SAA were supported by NASA Grant NNX11AH62G to the University of Wisconsin. The authors are grateful to G. Wind, G. T. Arnold, N. Amarasinghe, E. G. Moody, and B. A. Baum (cloud optical thickness and microphysical retriev-

als), R. A. Frey, L. E. Gumley, K. I. Strabala, and C. C. Moeller (cloud mask and cloud-top properties), and R. Pincus (level-3 design and early implementation), for software engineering, design, visualization, testing, and implementation of the MODIS cloud algorithms described in this paper. The authors continue to appreciate the support of the MODIS Characterization and Support Team (calibration and trending), and the MODIS Science Data Support Team (software integration, production, and data distribution).

REFERENCES

[1] S. A. Ackerman, K. I. Strabala, W. P. Menzel, R. A. Frey, C. C. Moeller, and L. E. Gumley, "Discriminating clear sky from clouds with MODIS," *J. Geophys. Res.*, vol. 103, no. D24, pp. 32141–32157, Dec. 1998.

[2] S. A. Ackerman, R. E. Holz, R. Frey, E. W. Eloranta, B. Maddux, and M. McGill, "Cloud Detection with MODIS: Part II Validation," *J. Atmos. Oceanic Technol.*, vol. 25, no. 7, pp. 10573–1086, Jul. 2008.

[3] W. L. Barnes, T. S. Pagano, and V. V. Salomonson, "Prelaunch characteristics of the Moderate Resolution Imaging Spectroradiometer (MODIS) on EOS-AM1," *IEEE Trans. Geosci. Remote Sens.*, vol. 36, no. 4, pp. 1088–1100, Jul. 1998.

[4] B. A. Baum, P. Yang, A. J. Heymsfield, S. Platnick, M. D. King, Y. X. Hu, and S. T. Bedka, "Bulk scattering properties for the remote sensing of ice clouds. Part II: Narrowband models," *J. Appl. Meteor.*, vol. 44, no. 12, pp. 1896–1911, Dec. 2005.

[5] R. A. Frey, B. A. Baum, W. P. Menzel, S. A. Ackerman, C. C. Moeller, and J. D. Spinhirne, "A comparison of cloud top heights computed from airborne lidar and MAS radiance data using CO_2 slicing," *J. Geophys. Res.*, vol. 104, no. D20, pp. 24547–24555, Oct. 1999.

[6] R. A. Frey, S. A. Ackerman, Y. Liu, K. I. Strabala, H. Zhang, J. Key, and X. Wang, "Cloud detection with MODIS, Part I: Recent improvements in the MODIS cloud mask," *J. Atmos. Oceanic Technol.*, vol. 25, no. 7, pp. 1057–1072, Jul. 2008.

[7] Q. Han, W. B. Rossow, and A. A. Lacis, "Near global survey of effective droplet radii in liquid clouds using ISCCP data," *J. Clim*ate, vol. 7, no. 4, pp. 465–497, Apr. 1994.

[8] R. E. Holz, S. A. Ackerman, F. W. Nagle, R. Frey, S. Dutcher, R. E. Kuehn, M. A. Vaughan, and B. Baum, "Global Moderate Resolution Imaging Spectroradiometer

(MODIS) cloud detection and height evaluation using CALIOP," *J. Geophys. Res.*, vol. 113, p. D00A19, Dec. 2008, DOI:10.1029/2008JD009837.

[9] P. A. Hubanks, "MODIS Atmosphere QA Plan for Collection 005," Greenbelt, MD, 59 pp., Oct. 30, 2006. [Online]. Available: http://modis-atmos.gsfc.nasa.gov/_docs/L3_ ATBD_2008_12_04.pdf.

[10] P. A. Hubanks, M. D. King, S. Platnick, and R. Pincus, "Cloud Atmosphere L3 Gridded Product Algorithm Theoretical Basis Document," Greenbelt, MD, 90 pp., Dec. 4, 2008. [Online]. Available: http://modis-atmos.gsfc.nasa.gov/_docs/L3_ ATBD_2008_12_04.pdf.

[11] M. D. King, Y. J. Kaufman, W. P. Menzel, and D. Tanré, "Remote sensing of cloud, aerosol, and water vapor properties from the Moderate Resolution Imaging Spectrometer (MODIS)," *IEEE Trans. Geosci. Remote Sens.*, vol. 30, no. 1, pp. 2–27, Jan. 1992.

[12] M. D. King, W. P. Menzel, Y. J. Kaufman, D. Tanré, B. C. Gao, S. Platnick, S. A. Ackerman, L. A. Remer, R. Pincus, and P. A. Hubanks, "Cloud and aerosol properties, precipitable water, and profiles of temperature and water vapor from MODIS," *IEEE Trans. Geosci. Remote Sens.*, vol. 41, no. 2, pp. 442–458, Feb. 2003.

[13] King, M. D., S. Platnick, G. Wind, G. T. Arnold, and R. T. Dominguez, "Remote sensing of the radiative and microphysical properties of clouds during TC^4: Results from MAS, MASTER, MODIS, and MISR," *J. Geophys. Res.*, vol. 115, p. D00J22, Jul. 2010, DOI:10.1029/2009JD013277.

[14] M. D. King, S. Platnick, P. Yang, G. T. Arnold, M. A. Gray, J. C. Riedi, S. A. Ackerman, and K. N. Liou, "Remote sensing of liquid water and ice cloud optical thickness and effective radius in the arctic: Application of airborne multispectral MAS data," *J. Atmos. Oceanic Technol.*, vol. 21, no. 6, pp. 857–875, Jun. 2004.

[15] M. D. King, S. Platnick, P. A. Hubanks, G. T. Arnold, E. G. Moody, G. Wind, and

B. Wind, "Collection 005 Change Summary for the MODIS Cloud Optical Properties (06_OD) Algorithm," Greenbelt, MD, May 9, 2006. [Online]. Available: http://modis-atmos.gsfc.nasa.gov/C005_Changes/C005_CloudOpticalProperties_ver311.pdf.

[16] A. A. Kokhanovsky, S. Platnick, and M. D. King, "Remote sensing of terrestrial clouds from space using backscattering and thermal emission techniques," in *The Remote Sensing of Tropospheric Composition from Space*, J. P. Burrows, U. Platt, and P. Borrell, Eds., pp. 231–257, Springer-Verlag, 2011.

[17] B. C. Maddux, S. A. Ackerman, and S. Platnick, "Viewing geometry dependencies in MODIS cloud products," *J. Atmos. Oceanic Technol.*, vol. 27, no. 9, pp. 1519–1528, Sep. 2010.

[18] W. P. Menzel, W. L. Smith, and T. R. Stewart, "Improved cloud motion wind vector and altitude assignment using VAS," *J. Appl. Meteor.*, vol. 22, no. 3, pp. 377–384, Mar. 1983.

[19] W. P. Menzel, D. P. Wylie, and K. I. Strabala, "Seasonal and diurnal changes in cirrus clouds as seen in four years of observations with the VAS," *J. Appl. Meteor.*, vol. 31, no. 4, pp. 370-385, Apr. 1992.

[20] W. P. Menzel, R. A. Frey, H. Zhang, D. P. Wylie, C. C. Moeller, R. E. Holz, B. Maddux, B. A. Baum, K. I. Strabala, and L. E. Gumley, "MODIS global cloud-top pressure and amount estimation: Algorithm description and results," *J. Appl. Meteor. Climatol.*, vol. 47, no. 4, pp. 1175–1198, Apr. 2008.

[21] N. Meskhidze, L. A. Remer, S. Platnick, R. N. Juárez, A. M. Lichtenberger, and A. R. Aiyyer, "Exploring the differences in cloud properties observed by the Terra and Aqua MODIS sensors," *Atmos. Chem. Phys.*, vol. 9, pp. 3461–3475, May 2009.

[22] P. Minnis, S. Sun-Mack, D. F. Young, P. W. Heck, D. P. Garber, Y. Chen, D. A. Spangenberg, R. F. Arduini, Q. Z. Trepte, W. L. Smith, Jr., J. K. Ayers, S. C. Gib-

son, W. F. Miller, G. Hong, V. Chakrapani, Y. Takano, K. N. Liou, Y. Xie, and P. Yang, "CERES edition-2 cloud property retrievals using TRMM VIRS and Terra and Aqua MODIS data—Part I: Algorithms," *IEEE Trans. Geosci. Remote Sens.*, vol. 49, no. 11, pp. 4374–4400, Nov. 2011.

[23] P. Minnis, S. Sun-Mack, Y. Chen, M. M. Khaiyer, Y. Yi, J. K. Ayers, R. R. Brown, X. Dong, S. C. Gibson, P. W. Heck, B. Lin, M. L. Nordeen, L. Nguyen, R. Palikonda, W. L. Smith, Jr., D. A. Spangenberg, Q. Z. Trepte, and B. Xi, "CERES edition-2 cloud property retrievals using TRMM VIRS and Terra and Aqua MODIS data—Part II: Examples of average results and comparisons with other data," *IEEE Trans. Geosci. Remote Sens.*, vol. 49, no. 11, pp. 4401–4430, Nov. 2011.

[24] P. Minnis, Q. Z. Trepte, S. Sun-Mack, Y. Chen, D. R. Doelling, D. F. Young, D. A. Spangenberg, W. F. Miller, B. A. Wielicki, R. R. Brown, S. C. Gibson, and E. B. Geier, "Cloud detection in nonpolar regions for CERES using TRMM VIRS and Terra and Aqua MODIS data," *IEEE Trans. Geosci. Remote Sens.*, vol. 46, no. 11, pp. 3857–3884, Nov. 2008.

[25] E. G. Moody, M. D. King, S. Platnick, C. B. Schaaf, and F. Gao, "Spatially complete global spectral surface albedos: Value-added datasets derived from Terra MODIS land products," *IEEE Trans. Geosci. Remote Sens.*, vol. 43, no. 1, pp. 144–158, Jan. 2005.

[26] E. G. Moody, M. D. King, C. B. Schaaf, D. K. Hall, and S. Platnick, "Northern Hemisphere five-year average (2000-2004) spectral albedos of surfaces in the presence of snow: Statistics computed from Terra MODIS land products," *Remote Sens. Environ.*, vol. 111, no. 3, pp. 337–345, Nov. 2007.

[27] E. G. Moody, M. D. King, C. B. Schaaf, and S. Platnick, "MODIS-derived spatially complete surface albedo products: Spatial and temporal pixel distribution and zonal averages," *J. Appl. Meteor. Climatol.*, vol. 47, no. 11, pp. 2879–2894, Nov. 2008.

[28] T. Nakajima, and M. D. King, "Determination of the optical thickness and effective particle radius of clouds from reflected solar radiation measurements. Part I: Theory," *J. Atmos. Sci.*, vol. 47, no. 15, pp. 894–907, Aug. 1990.

[29] T. Nakajima, M. D. King, J. D. Spinhirne, and L. F. Radke, "Determination of the optical thickness and effective particle radius of clouds from reflected solar radiation measurements. Part II: Marine stratocumulus observations," *J. Atmos. Sci.*, vol. 48, no. 5, pp. 728–750, Mar. 1991.

[30] T. Y. Nakajima, and T. Nakajima, "Wide-area determination of cloud microphysical properties from NOAA AVHRR measurements for FIRE and ASTEX regions," *J. Atmos. Sci.*, vol. 52, no. 23, pp. 4043–4059, Dec. 1995.

[31] T. Y. Nakajima, K. Suzuki, and G. L. Stephens, "Droplet growth in warm water clouds observed by the A-train: Part I: Sensitivity analysis of the MODIS-derived cloud droplet sizes," *J. Atmos. Sci.*, vol. 67, no. 6, pp. 1884–1896, Jun. 2010a.

[32] T. Y. Nakajima, K. Suzuki, and G. L. Stephens, "Droplet growth in warm water clouds observed by the A-train: Part II: A multisensor view," *J. Atmos. Sci.*, vol. 67, no. 6, pp. 1897–1907, Jun. 2010b.

[33] R. Pincus, S. Platnick, S. A. Ackerman, R. S. Hemler, and R. J. P. Hofmann, "Reconciling simulated and observed views of clouds: MODIS, ISCCP, and the limits of instrument simulators," *J. Climate*, vol. x, no. y, pp. xx-yy, month 2012.

[34] S. Platnick, "Vertical photon transport in cloud remote sensing problems," *J. Geophys. Res.*, vol. 105, no. D18, pp. 22919–22935, Sep. 2000.

[35] S. Platnick, and S. Twomey, "Determining the susceptibility of cloud albedo to changes in droplet concentration with the advanced very high resolution radiometer," *J. Appl. Meteor.*, vol. 33, no. 3, pp. 334–347, Mar. 1994.

[36] S. Platnick, J. Y. Li, M. D. King, H. Gerber, and P. V. Hobbs, "A solar reflectance method for retrieving cloud optical thickness and droplet size over snow and ice sur-

faces," *J. Geophys. Res.,* vol. 106, no. D14, pp. 15185–15199, Jul. 2001.

[37] S. Platnick, M. D. King, S. A. Ackerman, W. P. Menzel, B. A. Baum, J. C. Riedi, and R. A. Frey, " The MODIS cloud products: Algorithms and examples from Terra," *IEEE Trans. Geosci. Remote Sens.*, vol. 41, no. 2, pp. 459–473, Feb. 2003.

[38] W. B. Rossow, and A. A. Lacis, "Global, seasonal cloud variations from satellite radiance measurements. Part II: Cloud properties and radiative effects," *J. Climate*, vol. 3, no. 11, pp. 1204–1253, Nov. 1990.

[39] W. B. Rossow, and R. S. Schiffer, "ISCCP cloud data products," *Bull. Amer. Meteor. Soc.*, vol. 72, no. 1, pp. 2–20, Jan. 1991.

[40] W. B. Rossow, and R. S. Schiffer, "Advances in understanding clouds from ISCCP," *Bull. Amer. Meteor. Soc.*, vol. 80, no. 11, pp. 2261–2287, Nov. 1999.

[41] W. B. Rossow, A. W. Walker, and L. C. Gardner, "Comparison of ISCCP and other cloud amounts," *J. Climate*, vol. 6, no. 12, pp. 2394–2418, Dec. 1993.

[42] L. L. Stowe, E. P. McClain, R. Carey, P. Pellegrino, G. G. Gutman, P. Davis, C. Long, and S. Hart, "Global distribution of cloud cover derived from NOAA/AVHRR operational satellite data," *Adv. Space Res.*, vol. 11, no. 3, p. 51-54, Mar. 1991.

[43] K. Suzuki, T. Y. Nakajima, and G. L. Stephens, "Particle growth and drop collection efficiency of warm clouds as inferred from joint CloudSat and MODIS observations," *J. Atmos. Sci.*, vol. 67, no. 9, pp. 3019–3032, Sep. 2010.

[44] L. Wang, and A. E. Dessler, "Instantaneous cloud overlap statistics in the tropical area revealed by ICESat/GLAS data," *Geophys. Res. Lett.*, vol. 33, no. 8, p. L15804, DOI: 10.1029/2005GL024350, Aug. 2006.

[45] G. Wind, S. Platnick, M. D. King, P. A. Hubanks, M. J. Pavolonis, A. K. Heidinger, P. Yang, and B. A. Baum, "Multilayer cloud detection with the MODIS near-infrared water vapor absorption band," *J. Appl. Meteor. Climatol.*, vol. 49, no. 11, pp.

2315–2333, Nov. 2010.

[46] D. Wu, Y. Hu, M. P. McCormick, and F. Yan, "Global cloud-layer distribution statistics from 1 year CALIPSO lidar observations," *Int. J. Remote Sens.*, vol. 32, no. 5, pp. 1269–1288, Mar. 2011.

[47] D. P. Wylie, W. P. Menzel, H. M. Woolf, and K. I. Strabala, "Four years of global cirrus cloud statistics using HIRS," *J. Climate*, vol. 7, no. 12, pp. 1972–1986, Dec. 1994.

[48] D. P. Wylie, and W. P. Menzel, "Eight years of high cloud statistics using HIRS," *J. Climate*, vol. 12, no. 1, pp. 170–184, Dec. 1999.

[49] D. P. Wylie, D. L. Jackson, W. P. Menzel, and J. J. Bates, "Global cloud cover trends inferred from two decades of HIRS observations," *J. Climate*, vol. 18, no. 15, pp. 3021–3031, Aug. 2005.

[50] X. Xiong, J. Sun, W. Barnes, V. V. Salomonson, J. Esposito, H. Erives, and B. Guenther, "Multiyear on-orbit calibration and performance of Terra MODIS reflective solar bands," *IEEE Trans. Geosci. Remote Sens.*, vol. 45, no. 4, pp. 879–889, Apr. 2007.

[51] X. Xiong, B. N. Wenny, A. Wu, W. L. Barnes, and V. V. Salomonson, "Aqua MODIS thermal emissive band on-orbit calibration, characterization, and performance," *IEEE Trans. Geosci. Remote Sens.*, vol. 47, no. 3, pp. 803–814, Mar. 2009.

[52] P. Yang, Yang et al., "Differences Between Collection 4 and 5 MODIS Ice Cloud Optical/Microphysical Products and Their Impact on Radiative Forcing Simulations", *IEEE Trans. Geosci. Remote Sens.*, vol. 45, no. 9, pp. 2886-2899, Sept. 2007.

[53] Z. Zhang, and S. Platnick, "An assessment of differences between cloud effective particle radius retrievals for marine water clouds from three MODIS spectral bands," *J. Geophys. Res.*, vol. 116, p. D20215, DOI:10.1029/2011JD016216, Oct. 2011.

Michael D. King (M'01–SM'03) received the B.A. degree in physics from Colorado College in 1971, and the M.S. and Ph.D. degrees in atmospheric sciences from the University of Arizona, Tucson in 1973 and 1977, respectively.

From 1978 to 2008, he was a research scientist with the NASA Goddard Space Flight Center, Greenbelt, MD, where he served as Senior Project Scientist of NASA's Earth Observing System (EOS) from 1992-2008. Since April 2008, he has been a Senior Research Associate with the Laboratory for Atmospheric and Space Physics, University of Colorado Boulder. He is team leader of the MODIS Science Team. As a team member, he was responsible for developing the cloud optical and microphysical property and Level-3 algorithms. His research experience includes conceiving, developing, and operating multispectral scanning radiometers from a number of aircraft platforms in field experiments ranging from arctic stratus clouds to smoke from the Kuwait oil fires in the Persian Gulf and biomass burning in Brazil and southern Africa.

Dr. King is a Fellow of the American Geophysical Union (AGU) and American Meteorological Society (AMS), and a member of the U.S. National Academy of Engineering. He received the IEEE Prize Paper Award in 1993.

Steven Platnick received the B.S. degree in electrical engineering from Duke University in 1979, the M.S. degree in electrical engineering from the University of California Berkeley in 1980, and the Ph.D. degree in atmospheric sciences from the University of Arizona in 1991.

He joined NASA Goddard Space Flight Center in December 2002 and is currently EOS Senior Project Scientist. Prior to this appointment, he was a Research Associate Professor in the Joint Center for Earth Systems Technology, University of Maryland Baltimore County, from 1996-2002. He has worked in collaboration with NASA Goddard Space Flight Center since 1993, and prior to that held engineering positions at Hewlett-

Packard Co. for 6 years as well as a National Research Council Resident Research Associate position at NASA Ames Research Center. His research experience includes theoretical and experimental studies of satellite, aircraft, and ground-based cloud remote sensing, including applications to MODIS. He is a member of the MODIS Science Team and Atmospheric Discipline Team Leader.

W. Paul Menzel received the B.S. degree in physics from the University of Maryland, College Park, in 1967, and the M.S. and Ph.D. degrees in theoretical solid-state physics from the University of Wisconsin-Madison (UW), in 1968 and 1974, respectively.

In 1975 he joined the Space Science and Engineering Center at UW, where he was among the first to explore the possibilities for remote sensing of the Earth's atmosphere from a geosynchronous satellite. In 1983, he joined the National Oceanic and Atmospheric Administration (NOAA) National Environmental Satellite, Data, and Information Service (NESDIS), Madison, to lead the Advanced Satellite Products Team, where he was responsible for the development, testing, and evaluation of procedures for deriving new atmospheric products from spaceborne observations, which focused on transferring advances made in the research laboratory to the operational weather forecaster. Dr. Menzel was Chief Scientist for the Office of Research and Applications of NOAA/NESDIS from 1999-2006, and is currently a Senior Scientist in the Cooperative Institute for Meteorological Satellite Studies (CIMSS) at the University of Wisconsin, Madison. He is a member of the MODIS Science Team working on algorithms to derive cloud top properties, atmospheric profiles, and column water vapor using infrared bands.

Dr. Menzel is a Fellow of the American Meteorological Society (AMS). He received the IEEE Prize Paper Award in 1993.

Steven A. Ackerman received the B.S. degree in meteorology from the State University of New York, Oneonta, in 1976, and the M.S. and Ph.D. degrees in atmospheric science

from Colorado State University, in 1979 and 1987, respectively.

He is Professor of Atmospheric and Oceanic Sciences, University of Wisconsin, Madison, where he first joined the faculty in 1992. He is also the Director of the Cooperative Institute for Meteorological Satellite Studies (CIMSS), a position he has held since 1999. He is a member of the MODIS Science Team where he has primary responsibility for the MODIS cloud mask algorithm. His research experience includes remote sensing, radiative transfer, Earth radiation budgets, cloud radiative parameterizations, climate change; and aerosol studies. In addition to his participation in the MODIS Science Team, he is responsible for the cloud mask algorithm on the Visible Infrared Imaging Radiometer Suite (VIIRS), a sensor on NASA's National Polar-orbiting Operational Environmental Satellite System (NPOESS) Preparatory Project (NPP).

Paul A. Hubanks received the B.S. degree in mathematics from the University of Georgia in 1979 and completed two years in the M.S. meteorology program at Penn State University from 1979 to 1981.

He has more than 30 years' experience in satellite and aircraft data analysis and evaluation, solar and terrestrial research, scientific algorithm development and verification, software design-development-maintenance, data visualization, data analysis, and data management. In addition, he is an expert in designing and engineering state of the art world wide web sites and optimizing graphics and image data for the web, including the MODIS Atmosphere web site.

FIGURE LEGENDS

Fig. 1. Monthly mean cloud fraction (from cloud mask) for July 2006 from *Aqua* during (a) daytime and (b) nighttime.

Fig. 2 Seasonal mean daytime cloud fraction from *Terra* (2000-2011) and *Aqua* (2002-2011) for (a) December-February, (b) March-May, (c) June-August, and (d) September-November.

Fig. 3. Spatial distribution of daytime cloud fraction for *Aqua*–*Terra* for nine years (September 2002-August 2011) for (a) December-February, (b) March-May, (c) June-August, and (d) September-November, showing more clouds in the afternoon over land (*Aqua*) and in the morning over ocean (*Terra*).

Fig. 4. Zonal mean daytime cloud fraction over land (red) and ocean (blue) from *Terra* (2000-2011) and *Aqua* (2002-2011) for (a) December-February, (b) March-May, (c) June-August, and (d) September-November.

Fig. 5. Global mean daytime cloud fraction as a function of time for *Terra* and *Aqua* differentiated by surface type.

Fig. 6. Seasonal mean daytime cloud top pressure from *Terra* (2000-2011) and *Aqua* (2002-2011) for (a) December-February, (b) March-May, (c) June-August, and (d) September-November.

Fig. 7. Zonal mean daytime cloud top pressure over land (red) and ocean (blue) from *Terra* (2000-2011) and *Aqua* (2002-2011) for (a) December-February, (b) March-May, (c) June-August, and (d) September-November.

Fig. 8. Seasonal mean daytime cloud top temperature from *Terra* (2000-2011) and *Aqua* (2002-2011) for (a) December-February, (b) March-May, (c) June-August, and (d) September-November.

Fig. 9. Seasonal mean daytime cloud fraction from *Aqua* (2002-2011) for liquid water (left column) and ice (right column) clouds for (a) December-February, (b)

March-May, (c) June-August, and (d) September-November.

Fig. 10. Zonal and seasonal mean daytime cloud fraction from *Aqua* (2002-2011) for (a) liquid water clouds over land, (b) liquid water clouds over ocean, (c) ice clouds over land, and (d) ice clouds over ocean.

Fig. 11. Seasonal mean cloud optical thickness from *Aqua* (2002-2011) for liquid water (left column) and ice (right column) clouds for (a) December-February, (b) March-May, (c) June-August, and (d) September-November.

Fig. 12. Zonal and seasonal mean cloud optical thickness from *Aqua* (2002-2011) for (a) liquid water clouds over land, (b) liquid water clouds over ocean, (c) ice clouds over land, and (d) ice clouds over ocean.

Fig. 13. Seasonal mean cloud effective radius from *Aqua* (2002-2011) for liquid water (left column) and ice (right column) clouds for (a) December-February, (b) March-May, (c) June-August, and (d) September-November.

Fig. 14. Zonal and seasonal mean cloud effective radius from *Aqua* (2002-2011) for (a) liquid water clouds over land, (b) liquid water clouds over ocean, (c) ice clouds over land, and (d) ice clouds over ocean.

Fig. 15. Probability density function of cloud optical thickness of (a) liquid water and (b) ice clouds over both land and ocean for *Terra* and *Aqua* during July 2006. Panels (c) and (d) show corresponding probability density function of cloud effective radius of liquid water and ice clouds. Note that "means" don't mean a thing when the distribution is highly skewed, as is the case for the cloud optical thickness and, to a lesser extent, effective radius of liquid water clouds. These results correspond to global clouds from 90°N to 90°S.

Fig. 16. Monthly joint histograms of cloud optical thickness and effective radius for liquid water clouds over the ocean between 32°-40°N and 117°-125°W for (a) *Terra* and (b) *Aqua* for July 2006, and between 12°-24°S and 68°-80°W for (c) *Terra*

and (d) *Aqua* for September 2006. Note the somewhat smaller cloud optical thickness values in the afternoon, consistent with the normal diurnal cycle for marine stratocumulus clouds off both California (a-b) and Peru (c-d).

Fig. 17. Monthly joint histograms of cloud optical thickness and cloud top pressure between 50°N and 50°S for August 2001 from *Terra*. Panel (a) is for ISCCP-like cloud top pressure and cloud optical thickness boundaries, and panels (b) and (c) are for liquid water and ice clouds using a finer discretization in cloud top pressure and cloud optical thickness based on the MODIS collection 5 algorithm.

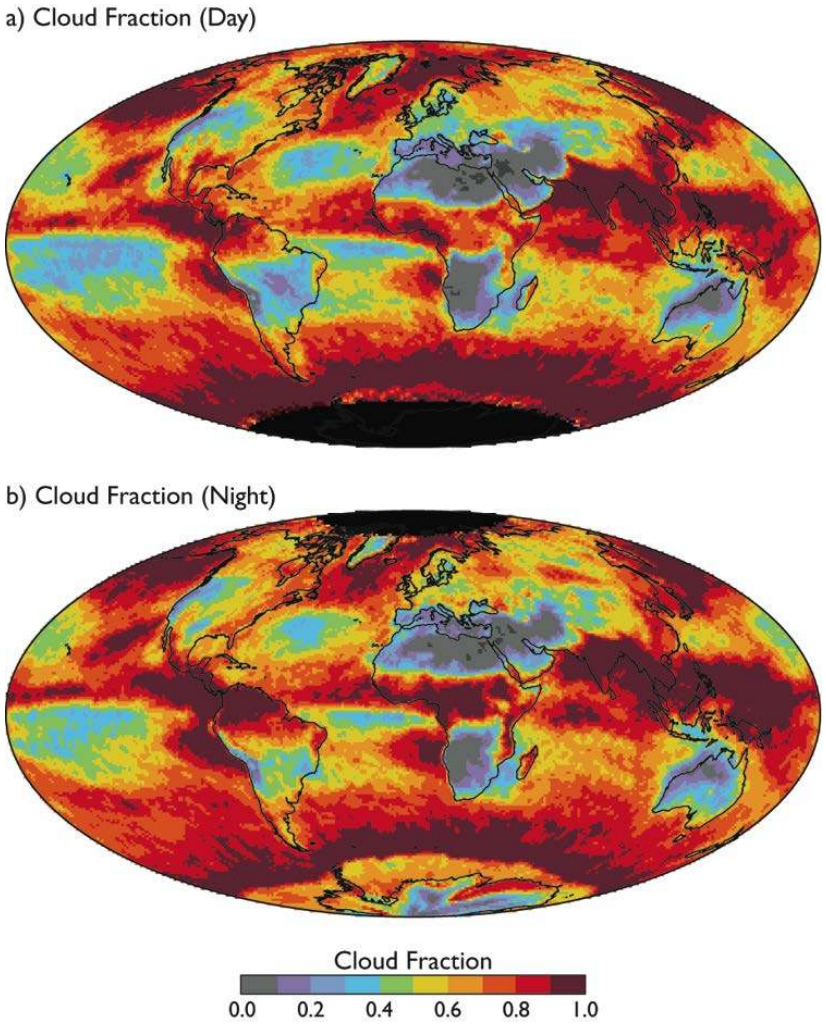

Fig. 1. Monthly mean cloud fraction (from cloud mask) for July 2006 from *Aqua* during (a) daytime and (b) nighttime.

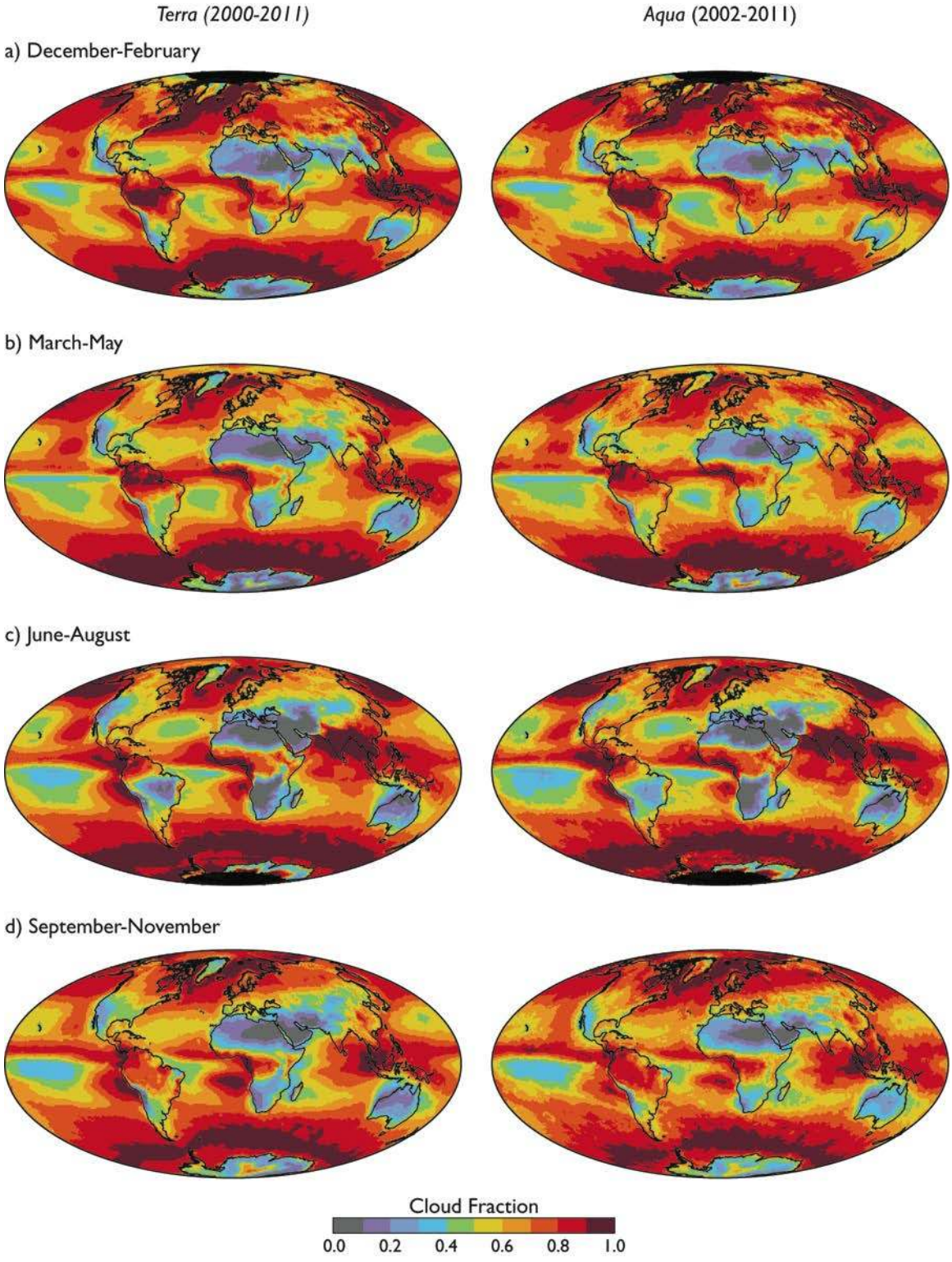

Fig. 2. Seasonal mean daytime cloud fraction from *Terra* (2000-2011) and *Aqua* (2002-2011) for (a) December-February, (b) March-May, (c) June-August, and (d) September-November.

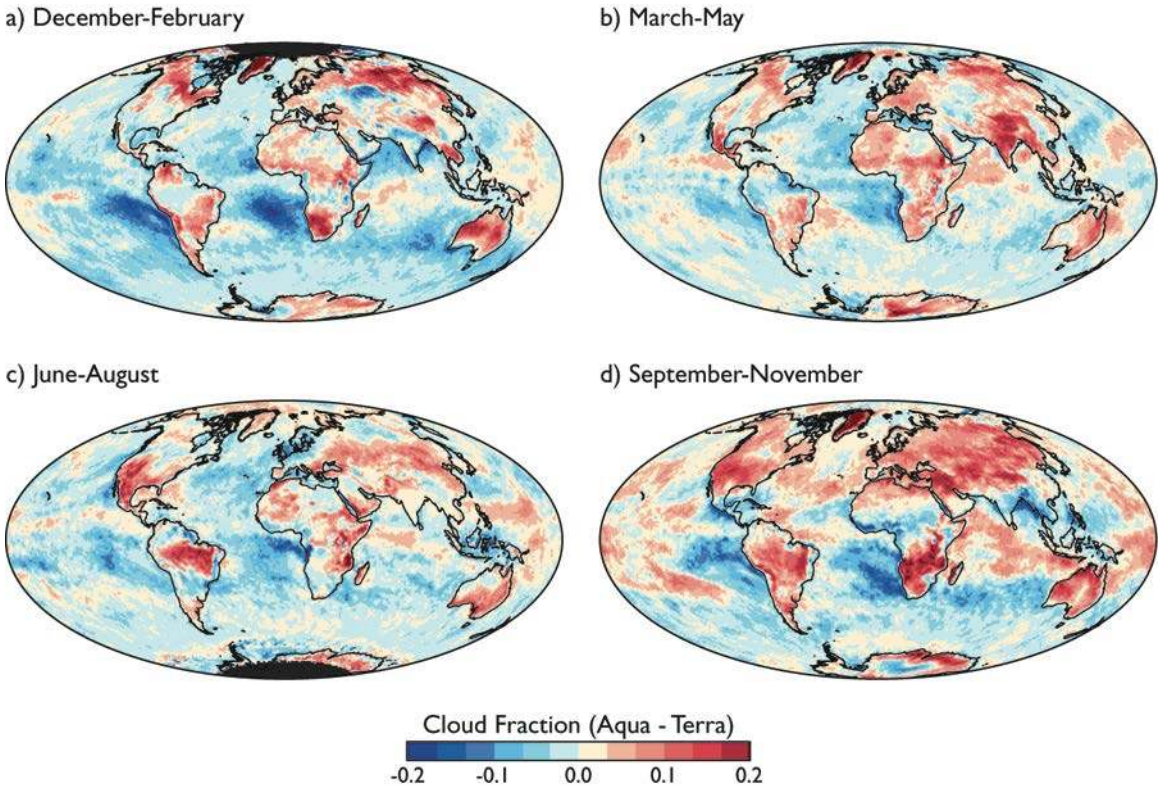

Fig. 3. Spatial distribution of daytime cloud fraction for *Aqua–Terra* for nine years (September 2002-August 2011) for (a) December-February, (b) March-May, (c) June-August, and (d) September-November, showing more clouds in the afternoon over land (*Aqua*) and in the morning over ocean (*Terra*).

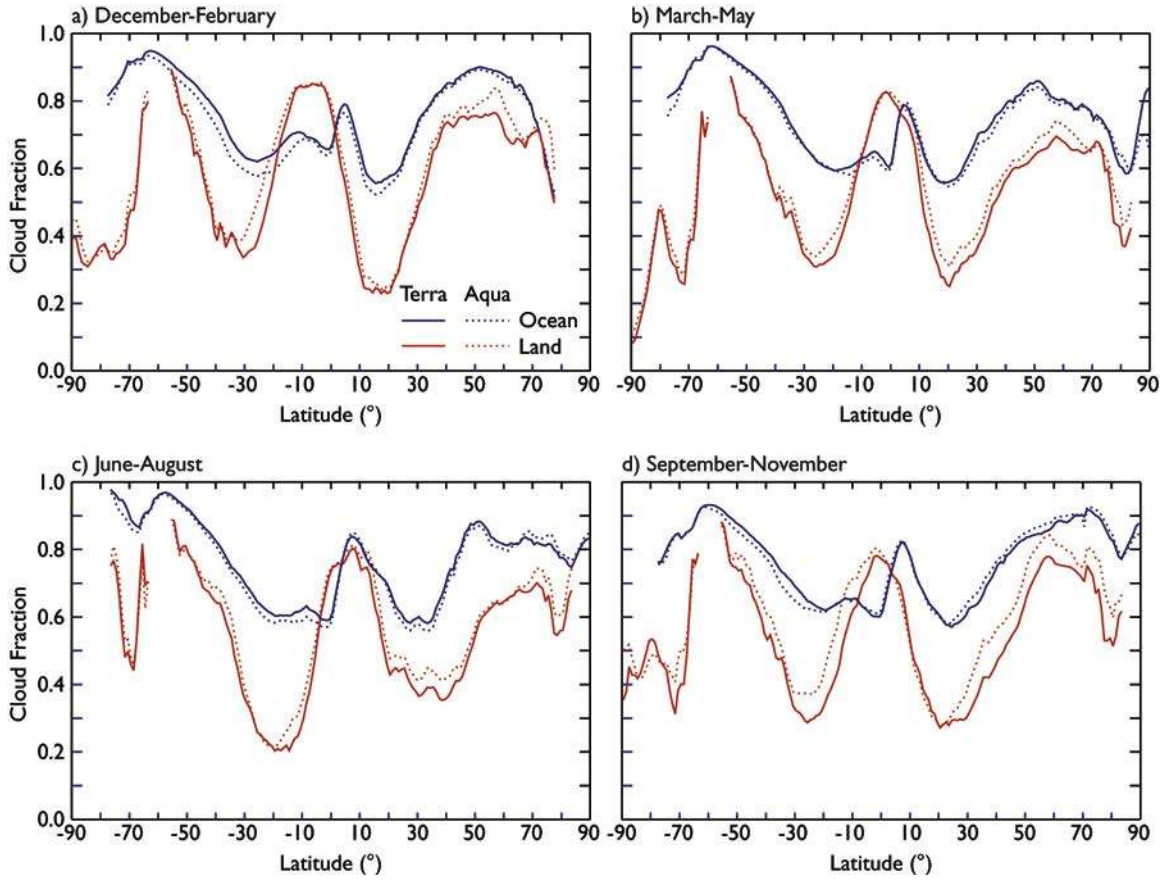

Fig. 4. Zonal mean daytime cloud fraction over land (red) and ocean (blue) from *Terra* (2000-2011) and *Aqua* (2002-2011) for (a) December-February, (b) March-May, (c) June-August, and (d) September-November.

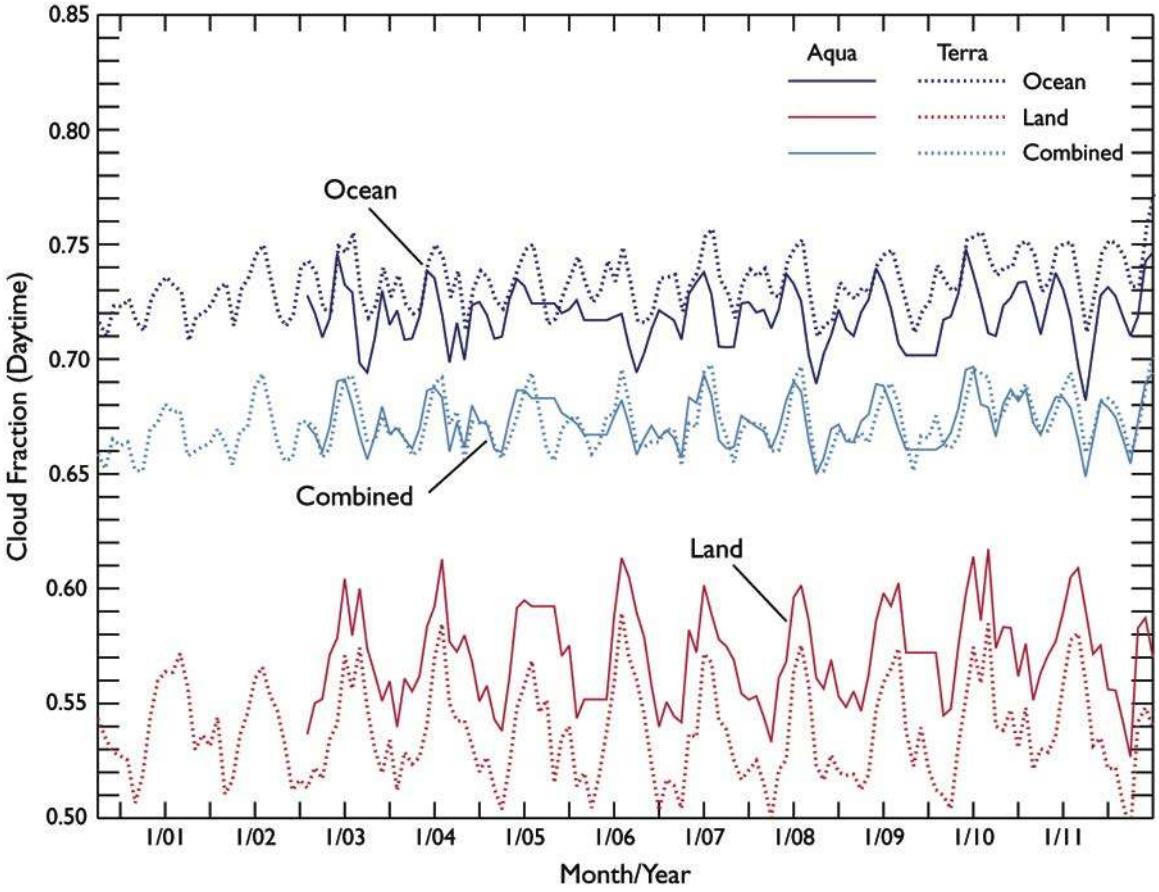

Fig. 5. Global mean daytime cloud fraction as a function of time for *Terra* and *Aqua* differentiated by surface type.

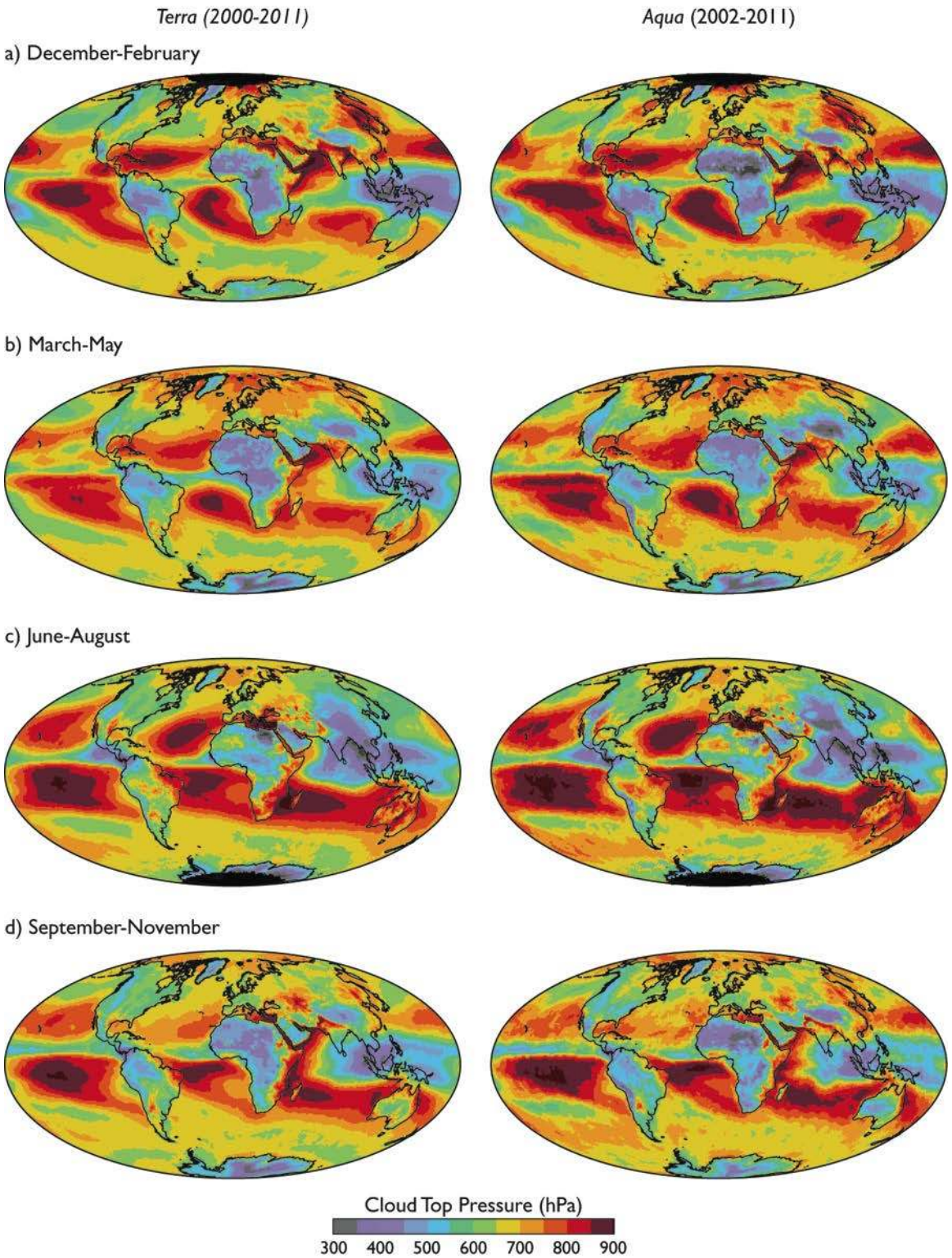

Fig. 6. Seasonal mean daytime cloud top pressure from *Terra* (2000-2011) and *Aqua* (2002-2011) for (a) December-February, (b) March-May, (c) June-August, and (d) September-November.

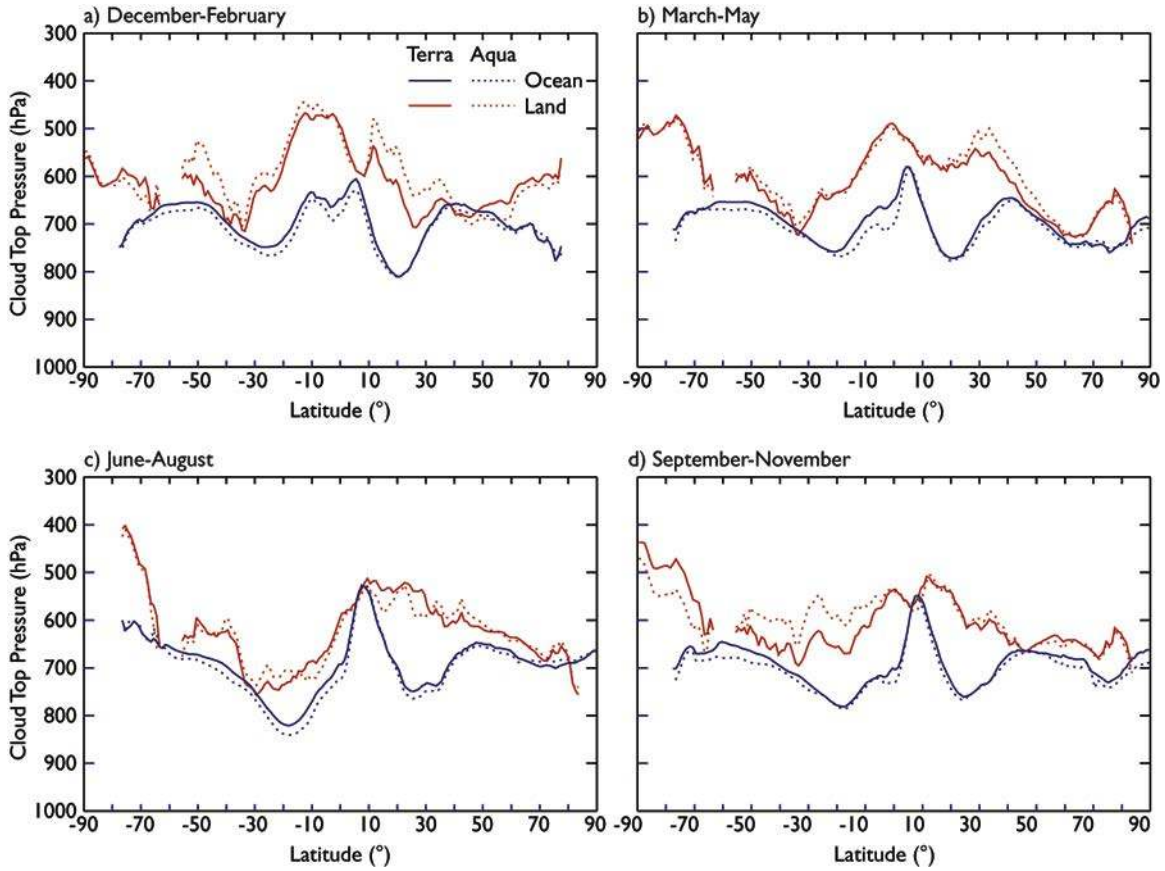

Fig. 7. Zonal mean daytime cloud top pressure over land (red) and ocean (blue) from *Terra* (2000-2011) and *Aqua* (2002-2011) for (a) December-February, (b) March-May, (c) June-August, and (d) September-November.

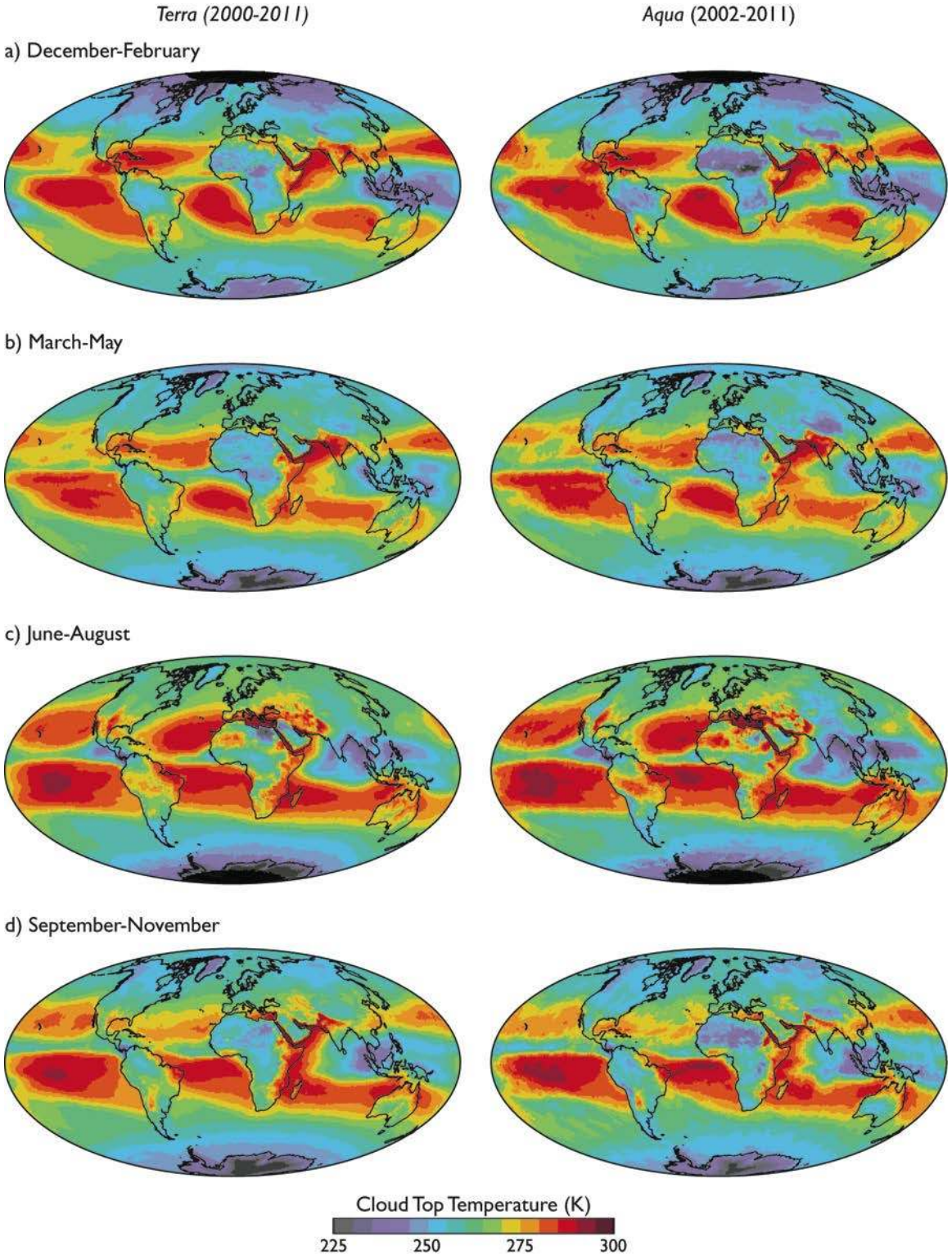

Fig. 8. Seasonal mean daytime cloud top temperature from *Terra* (2000-2011) and *Aqua* (2002-2011) for (a) December-February, (b) March-May, (c) June-August, and (d) September-November.

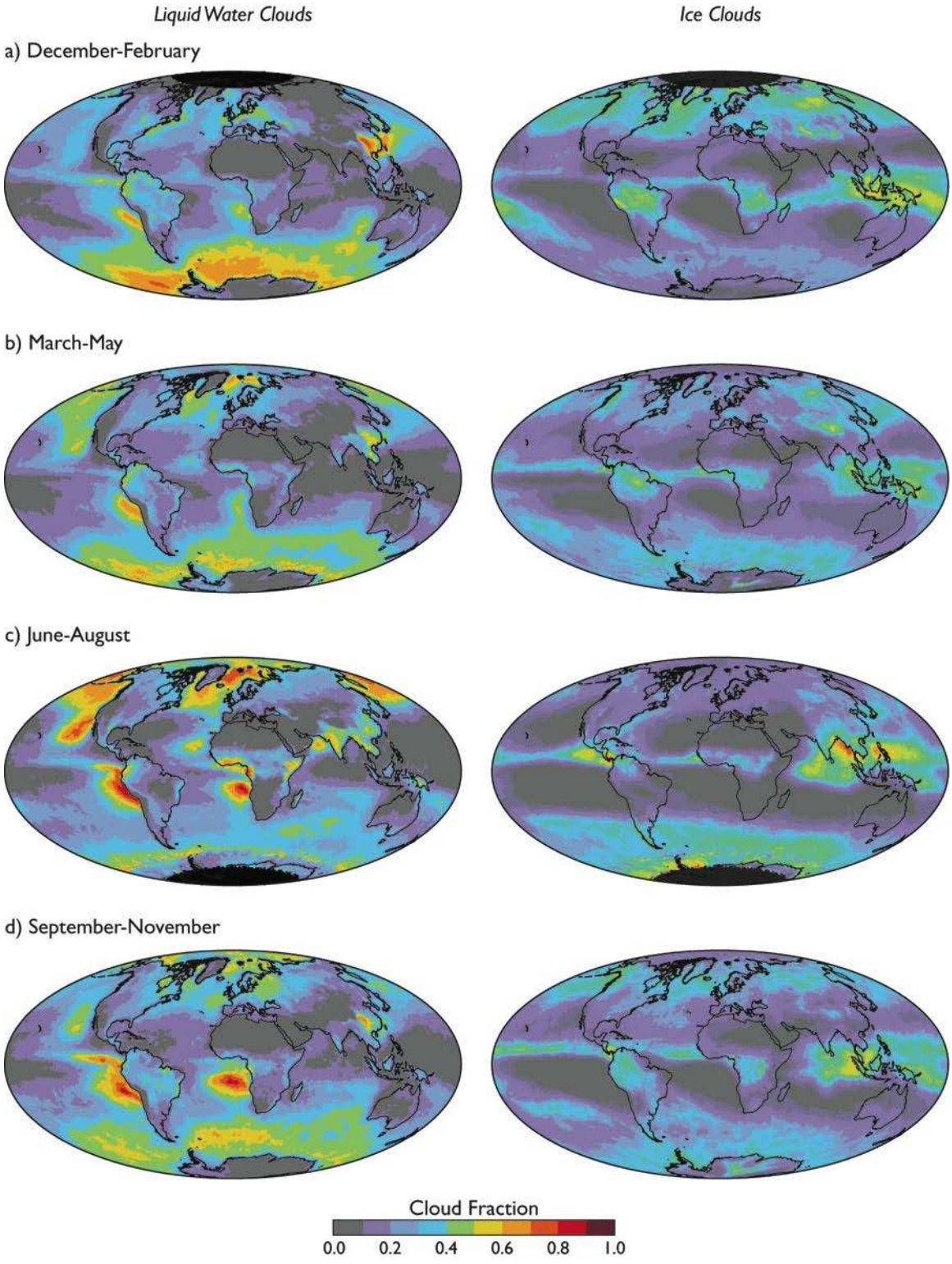

Fig. 9. Seasonal mean daytime cloud fraction from *Aqua* (2002-2011) for liquid water (left column) and ice (right column) clouds for (a) December-February, (b) March-May, (c) June-August, and (d) September-November.

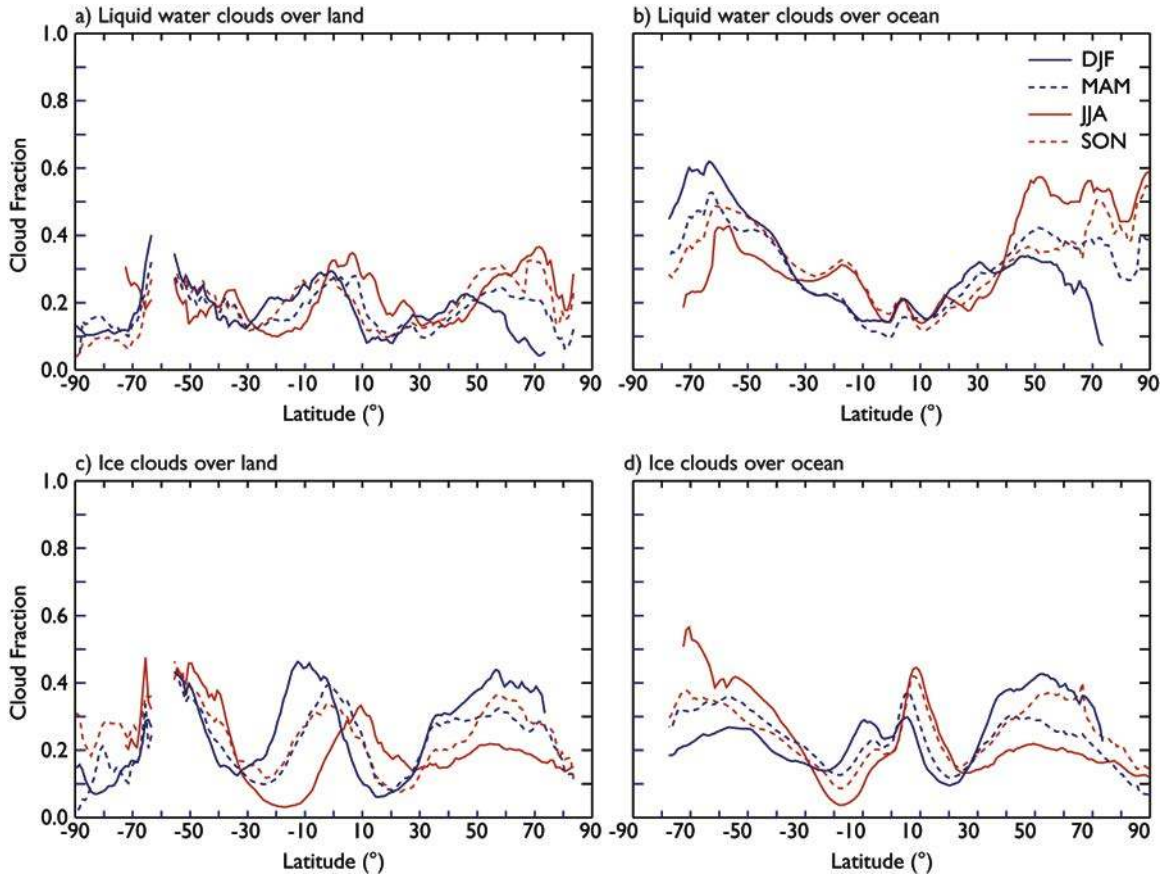

Fig. 10. Zonal and seasonal mean daytime cloud fraction from *Aqua* (2002-2011) for (a) liquid water clouds over land, (b) liquid water clouds over ocean, (c) ice clouds over land, and (d) ice clouds over ocean.

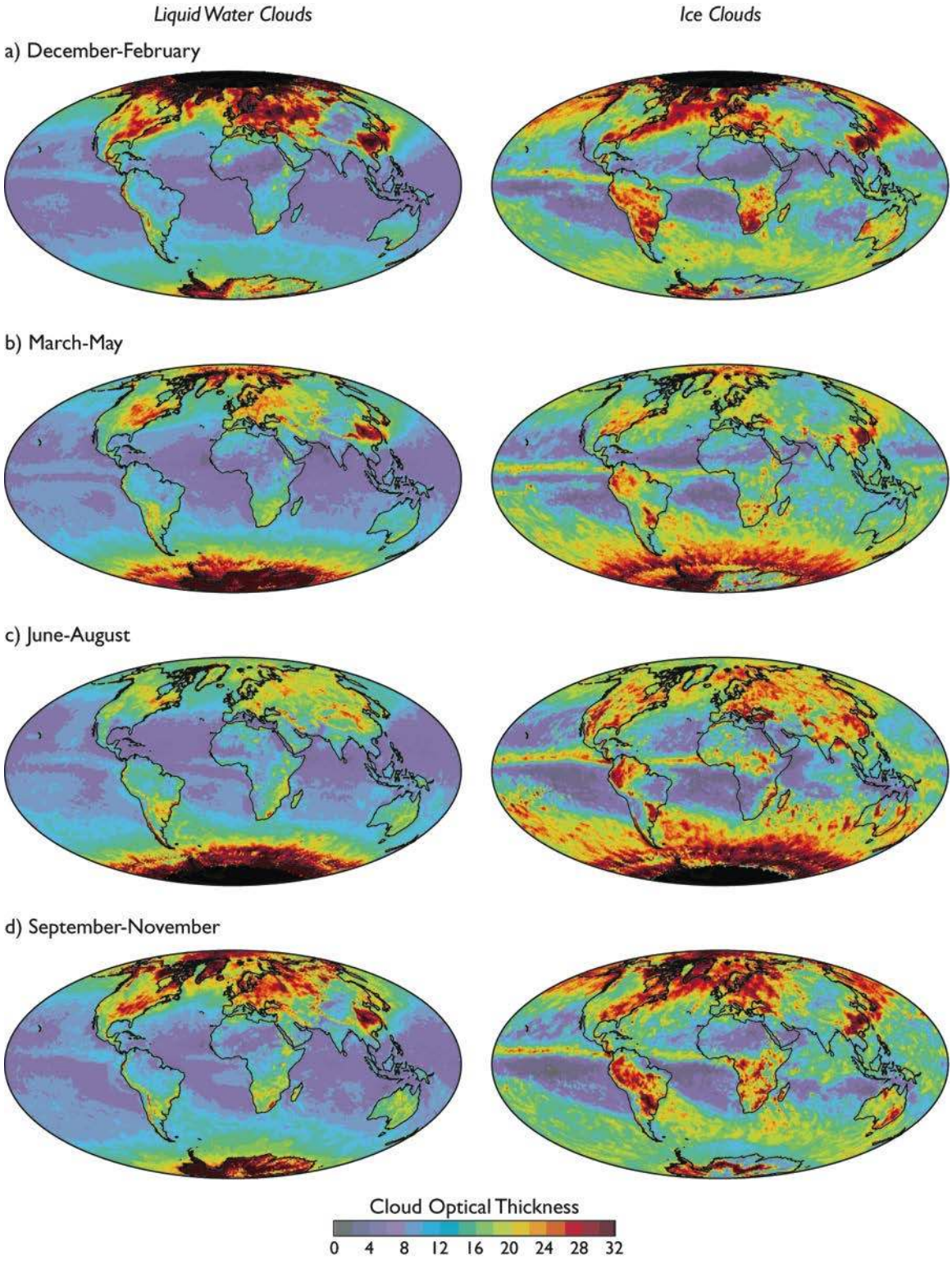

Fig. 11. Seasonal mean cloud optical thickness from *Aqua* (2002-2011) for liquid water (left column) and ice (right column) clouds for (a) December-February, (b) March-May, (c) June-August, and (d) September-November.

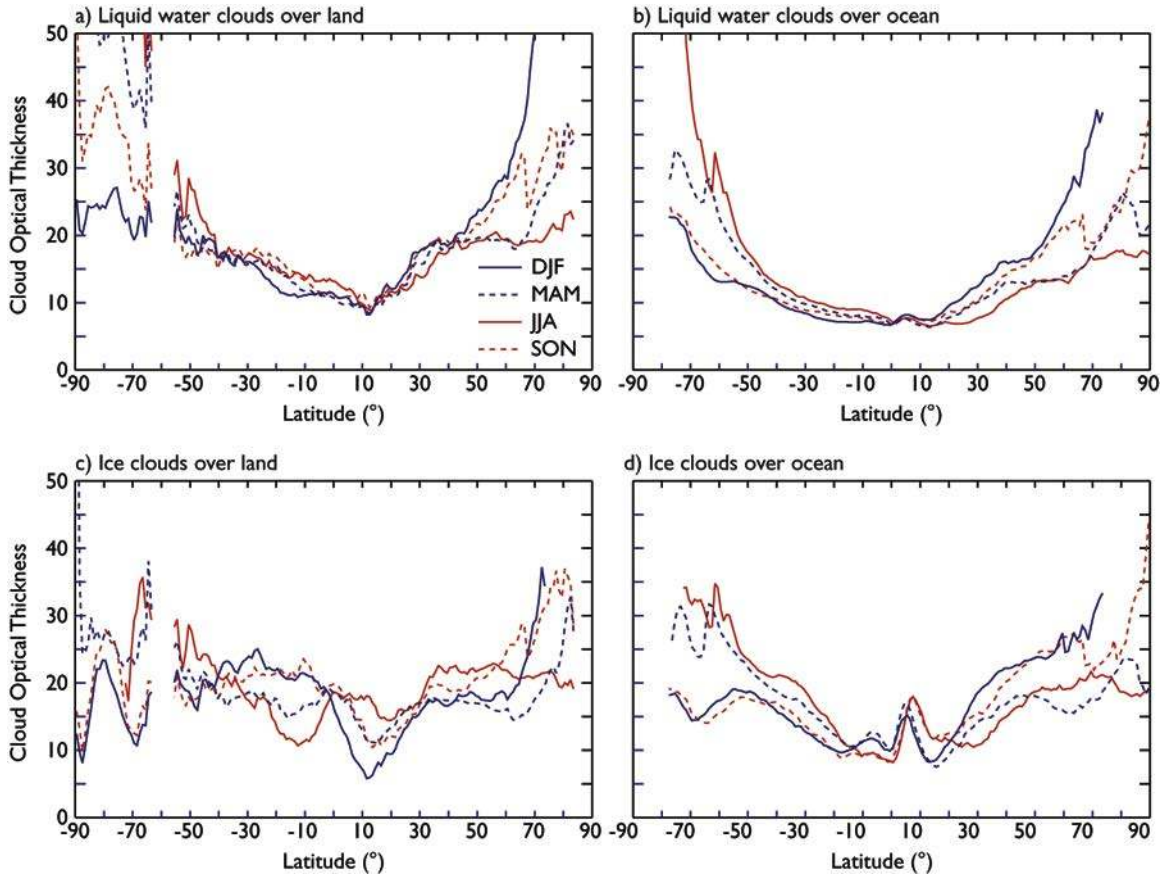

Fig. 12. Zonal and seasonal mean cloud optical thickness from *Aqua* (2002-2011) for (a) liquid water clouds over land, (b) liquid water clouds over ocean, (c) ice clouds over land, and (d) ice clouds over ocean.

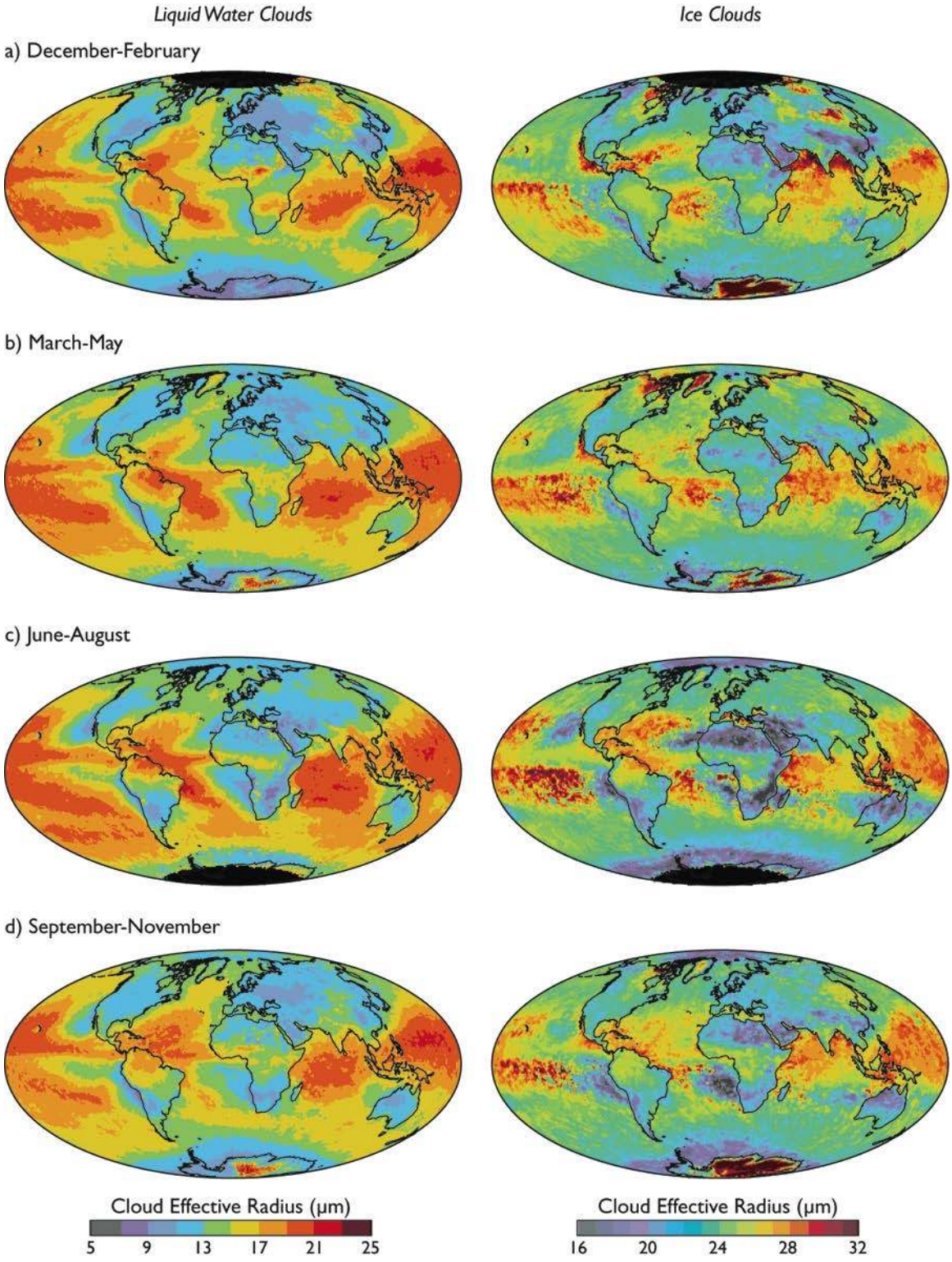

Fig. 13. Seasonal mean cloud effective radius from *Aqua* (2002-2011) for liquid water (left column) and ice (right column) clouds for (a) December-February, (b) March-May, (c) June-August, and (d) September-November.

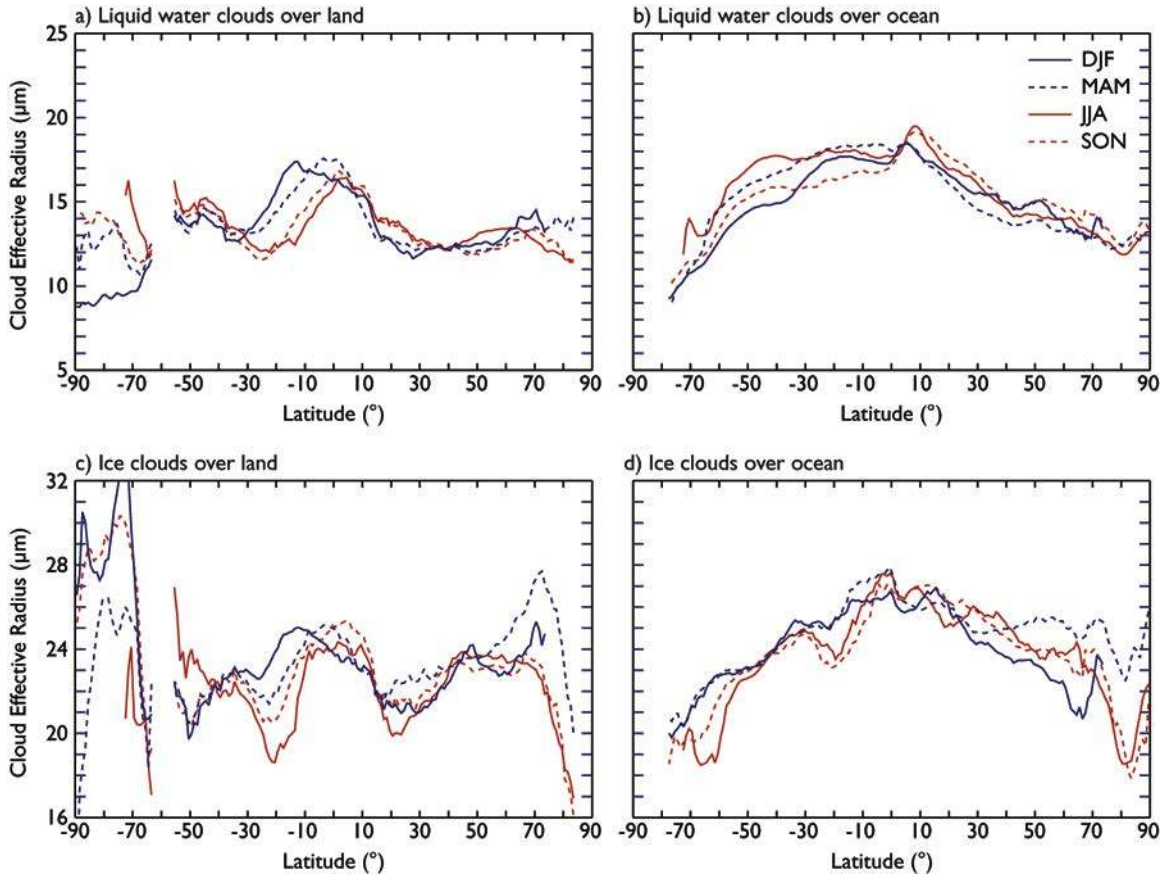

Fig. 14. Zonal and seasonal mean cloud effective radius from *Aqua* (2002-2011) for (a) liquid water clouds over land, (b) liquid water clouds over ocean, (c) ice clouds over land, and (d) ice clouds over ocean.

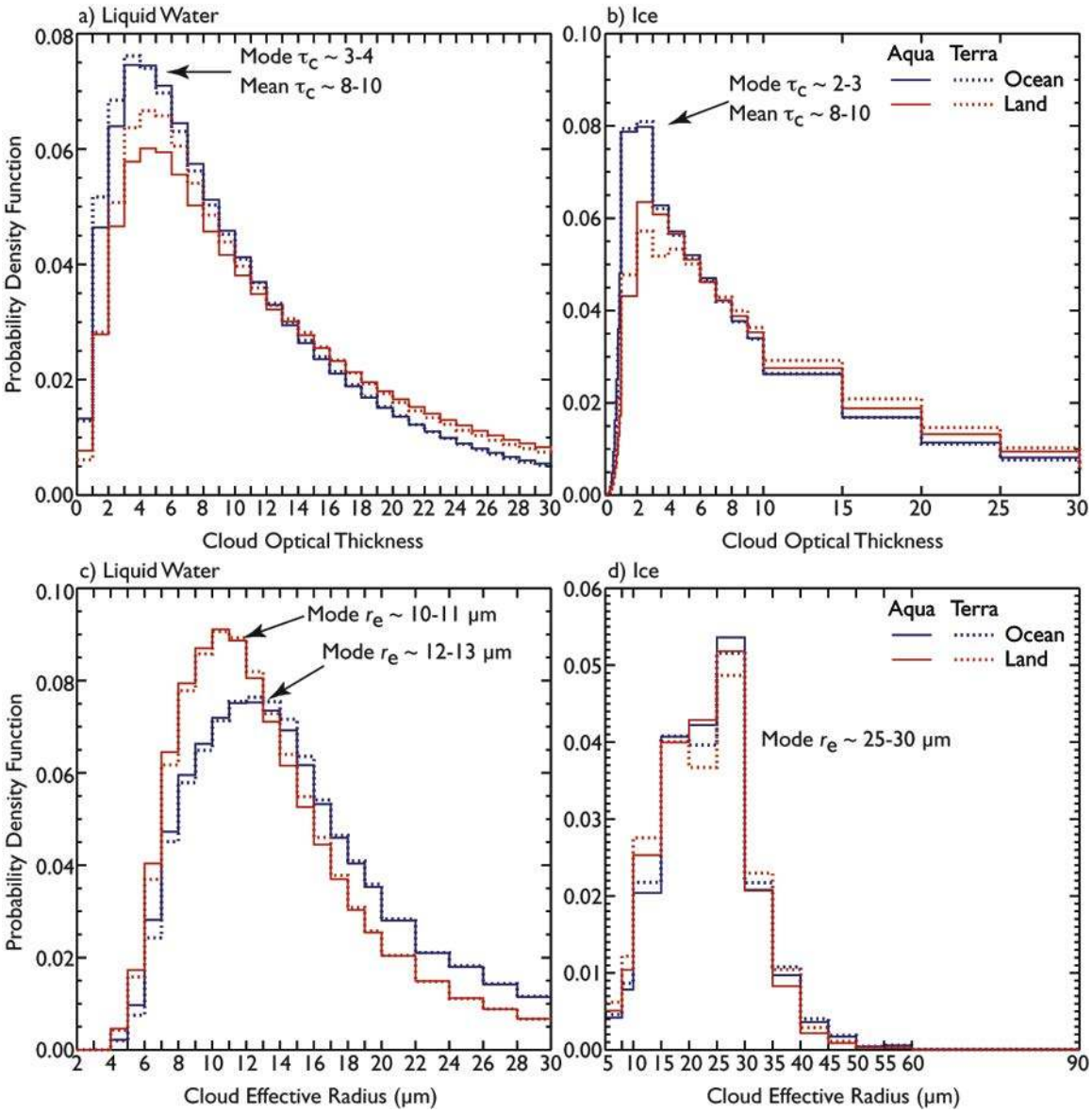

Fig. 15. Probability density function of cloud optical thickness of (a) liquid water and (b) ice clouds over both land and ocean for *Terra* and *Aqua* during July 2006. Panels (c) and (d) show corresponding probability density function of cloud effective radius of liquid water and ice clouds. Note that mean values are not a sufficient metric when the distribution is highly skewed, as is the case for the cloud optical thickness and, to a lesser extent, effective radius of liquid water clouds. These results correspond to global clouds from 90°N to 90°S.

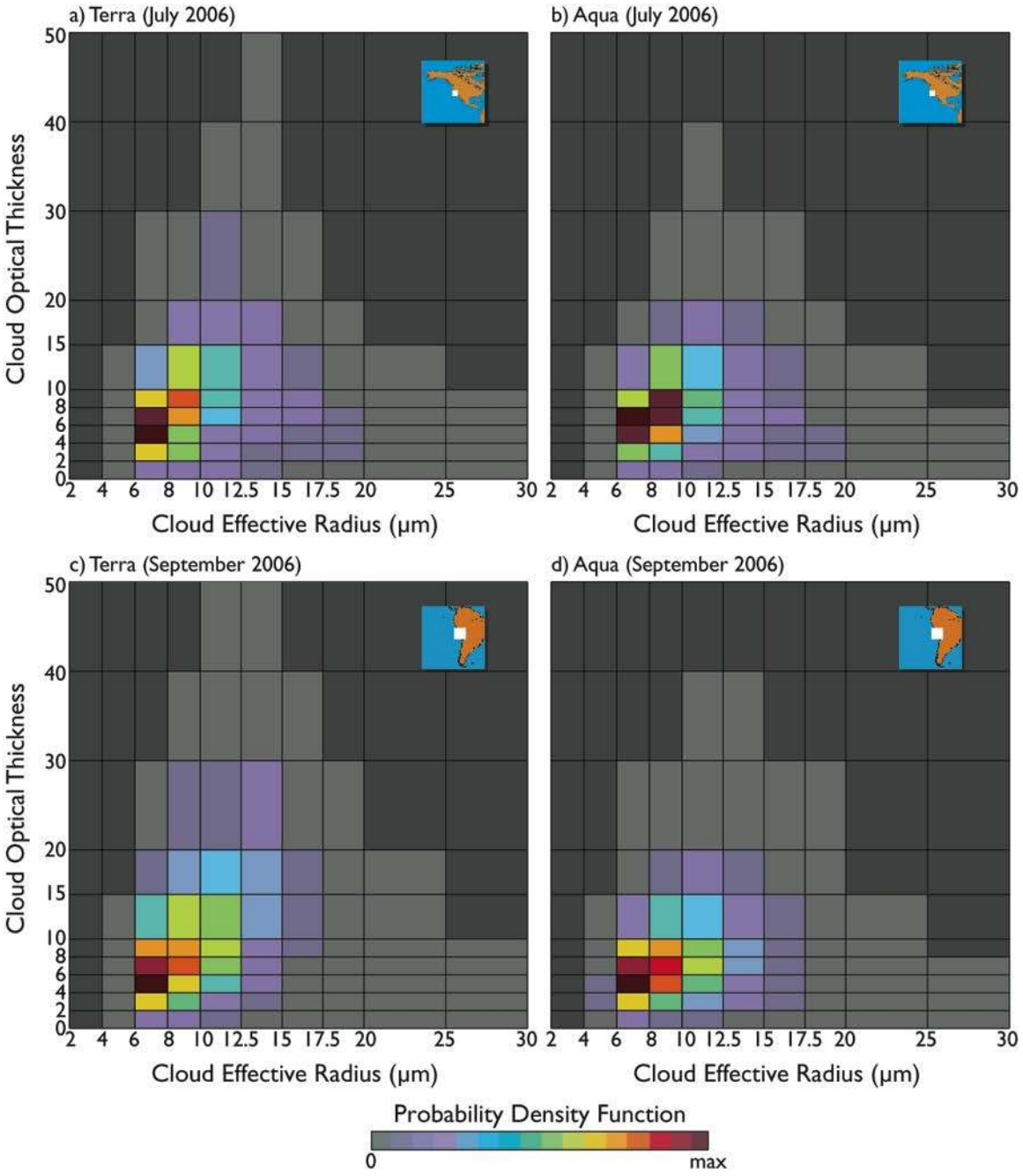

Fig. 16. Monthly joint histograms of cloud optical thickness and effective radius for liquid water clouds over the ocean between 32°-40°N and 117°-125°W for (a) *Terra* and (b) *Aqua* for July 2006, and between 12°-24°S and 68°-80°W for (c) *Terra* and (d) *Aqua* for September 2006. Note the somewhat smaller cloud optical thickness values in the afternoon, consistent with the normal diurnal cycle for marine stratocumulus clouds off both California (a-b) and Peru (c-d).

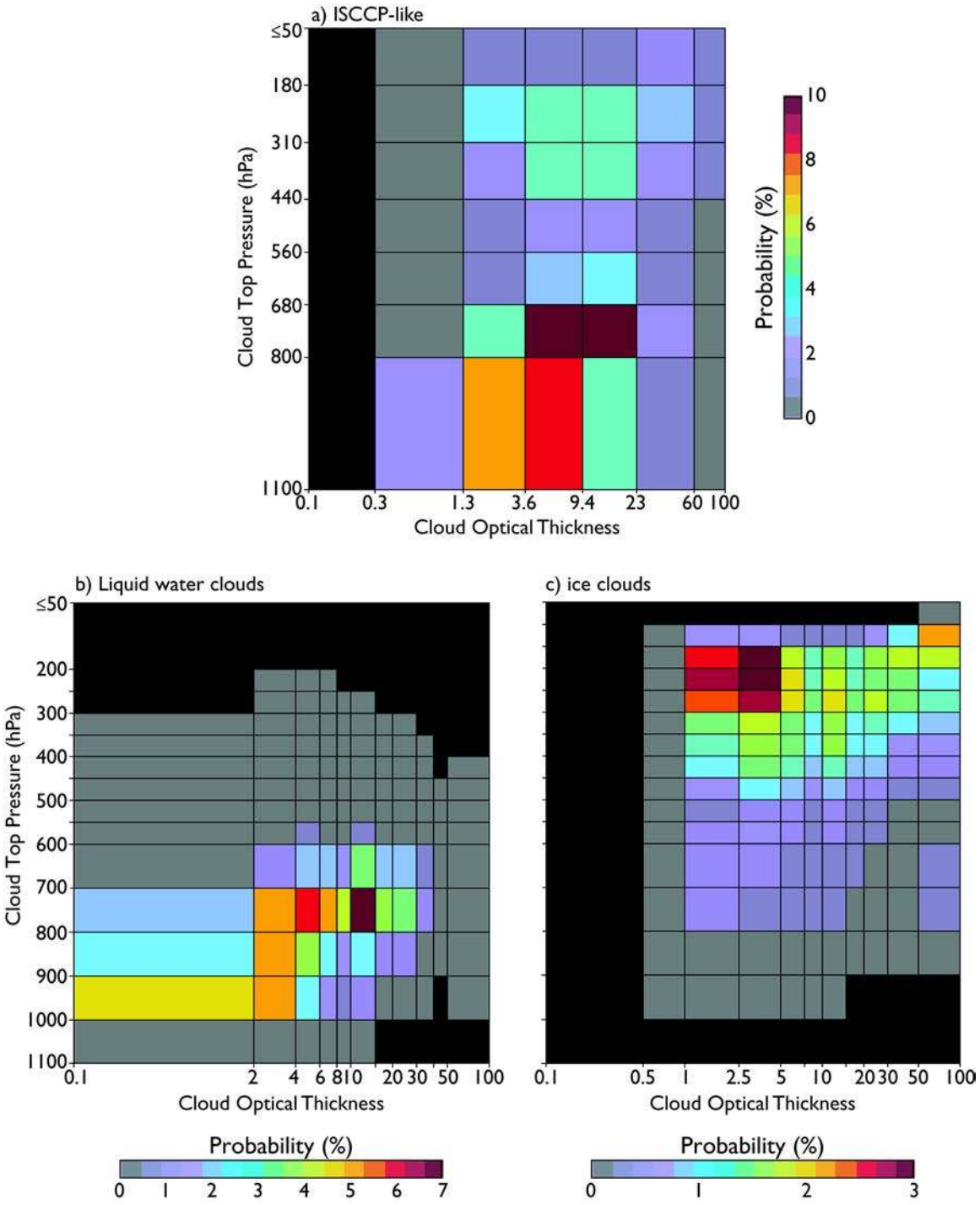

Fig. 17. Monthly joint histograms of cloud optical thickness and cloud top pressure between 50°N and 50°S for August 2001 from *Terra*. Panel (a) is for ISCCP-like cloud top pressure and cloud optical thickness boundaries, and panels (b) and (c) are for liquid water and ice clouds using a finer discretization in cloud top pressure and cloud optical thickness based on the MODIS collection 5 algorithm.